Geol. Mag. **148** (*5–6*), *2011, pp. 980–1008.* © *Cambridge University Press 2011*
doi:10.1017/S0016756811000380

Post-collisional polycyclic plutonism from the Zagros hinterland: the Shaivar Dagh plutonic complex, Alborz belt, Iran

MEHRAJ AGHAZADEH*, ANTONIO CASTRO‡†, ZAHRA BADRZADEH*
& KATHARINA VOGT§

*Department of Geology, University of Payam Noor, Iran
‡Department of Geology, University of Huelva, Spain
§Institute of Geophysics, ETH-Zürich, Switzerland

(*Received* 29 September 2010; *accepted* 7 February 2011; *first published online* 24 June 2011)

Abstract – The petrological and geochronological study of the Cenozoic Shaivar Dagh composite intrusion in the Alborz Mountain belt (NW Iran) reveals important clues to decipher complex relations between magmatic and tectonic processes in the central sectors of the Tethyan (Alpine–Himalayan) orogenic belt. This pluton is formed by intrusion at different times of two main magmatic cycles. The older (Cycle 1) is formed by calc-alkaline silicic rocks, which range in composition from diorites to granodiorites and biotite granites, with abundant mafic microgranular enclaves. The younger cycle (Cycle 2) is formed by K-rich monzodiorite and monzonite of marked shoshonitic affinity. The latter form the larger volumes of the exposed plutonic rocks in the studied complex. Zircon geochronology (laser ablation ICP-MS analyses) gives a concordia age of 30.8 ± 2.1 Ma for the calc-alkaline rocks (Cycle 1) and a range from 23.3 ± 0.5 to 25.1 ± 0.9 Ma for the shoshonitic association (Cycle 2). Major and trace element relations strongly support distinct origins for each magmatic cycle. Rocks of Cycle 1 have all the characteristic features of active continental margins. Shoshonitic rocks (Cycle 2) define two continuous fractionation trends: one departing from a K-rich basaltic composition and the other from an intermediate, K-rich composition. A metasomatized-mantle origin for the two shoshonitic series of Cycle 2 is proposed on the basis of comparisons with experimental data. The origin of the calc-alkaline series is more controversial but it can be attributed to processes in the suprasubduction mantle wedge related to the incorporation of subducted mélanges in the form of silicic cold plumes. A time sequence can be established for the processes responsible of the generation of the two magmatic cycles: first a calc-alkaline cycle typical of active continental margins, and second a K-rich cycle formed by monzonites and monzodiorites. This sequence precludes the younger potassic magmas as precursors of the older calc-alkaline series. By contrast, the older calc-alkaline magmas may represent the metasomatic agents that modified the mantle wedge during the last stages of subduction and cooked a fertile mantle region for late potassic magmatism after continental collision.

Keywords: Zagros orogen, monzonite, subduction, post-collisional, calc-alkaline.

1. Introduction

The tectonic evolution of collisional orogenic belts is typically marked by changes in the composition of the associated magmatic rocks (e.g. Harris, Pearce & Tindele, 1986). Consequently, the study of magmatic rocks is crucial to reconstruct processes occurring before and after collision, and to understand the role of these processes in the generation of distinct types of magmatism. Although many studies have been focused on finding a relationship between tectonic and magmatic processes in collisional orogens, important questions still remain unsolved. For instance, the volumetrically most important magmatic activity in collisional orogens is produced several million years (about 10–30 Ma) later with respect to the main tectonic episodes. The so-called post-collisional magmatism is the most characteristic petrologic feature of many, but not all, orogenic environments related to continent–continent collision. The establishment of robust petrogenetic and tectonic models needs a precise knowledge of the timing relationships between magmatism and tectonic processes, and this timing is still not well constrained in the Zagros orogenic belt. Key questions for understanding the relation between magmatism and tectonic processes in collisional orogens are: Is lithosphere extension associated with post-collisional uplift the process responsible for magmatic activity? Are magmas generated by decompression melting of previously thickened continental crust? Is the mantle involved in granite magmatism during decompression? The answers need the understanding of petrogenetic processes and the detailed knowledge of phase equilibria that determine geochemical features of magmas. The main feature of post-collisional intrusive complexes is the association of calc-alkaline, high-K calc-alkaline and potassic (shoshonitic) to ultrapotassic magmatic rocks, which are closely related in space and time. These associations have been reported in several orogenic belts, such as the Palaeoproterozoic Svecofennian (Eklund *et al.* 1998), Neoproterozoic East African (Küster & Harms, 1998), Appalachian

---

†Author for correspondence: dorado@uhu.es

(Venturelli *et al.* 1984), Hercynian (Ajaji *et al.* 1998; López-Moro & López-Plaza, 2004) and Himalayan (Turner *et al.* 1996; Williams *et al.* 2004; Gao *et al.* 2010) belts. Several studies have been performed on the Zagros belt supplying valuable information about petrogenesis and age relationships of magmatism (Haschke *et al.* 2010).

Collisional orogenic belts contain invaluable structural, sedimentary and magmatic records of the geological history of the Earth and, therefore, they have attracted the attention of earth scientists. One of the most studied collisional orogens is the Tethyan belt (Şengör & Kidd, 1979; Turner *et al.* 1996; Gao *et al.* 2010) extending from the Alps to the Himalayas. Large portions of this belt are characterized by complex collisional processes involving continental blocks that were separated from the northern Gondwana margin (Stocklin, 1974; Berberian & King, 1981; Stampfli, 2000). The Zagros orogenic belt, which extends for more than 2000 km in Central Iran (Alavi, 2004), is among the most interesting portions of this huge tectonic belt. In spite of the presence of several well-developed magmatic alignments, such as the Urumieh–Dokhtar and Sanandaj–Sirjan magmatic zones, associated with varied tectonic styles, namely subduction, collision and post-collision, this portion of the Tethyan orogen is still poorly known from the point of view of magmatism. New petrological data about complex and polycyclic intrusions from the northwesternmost portion of the Zagros–Alborz orogenic systems are reported here for the first time with the aim of contributing to the better understanding of the tectonic evolution of this important sector of the Tethyan orogen. The presence of post-tectonic voluminous plutonic intrusions of K-rich magmas, and their association with almost coeval magma pulses of typical calc-alkaline composition, makes this area in Iran of particular relevance to test petrogenetic and tectonic models. Here, we show a petrological and geochronological preliminary study of intrusive rocks of this sector of the Zagros hinterland in Iran. This study includes major and trace element geochemistry, Sr–Nd isotopic signatures and zircon U–Pb geochronology of high-K calc-alkaline and shoshonitic plutonic associations that form the Shaivar Dagh intrusive complex (SDIC) in the NW part of the Alborz mountain belt (AMB, Fig. 1a). The new petrological and geochronological data reported in this paper are interpreted within the constraints imposed by laboratory experiments and numerical thermo-mechanical models for subduction systems. These provide a new scenario for arc-related and post-collisional magmatism leading to a better understanding of the complex evolution in this sector of the Tethyan orogen.

2. Outline of regional geology

Repeated accretion and collision events of continental fragments and intra-oceanic magmatic arcs have formed the complex architecture of the Zagros orogen during the Mesozoic and Tertiary. Two main collision periods can be recognized. The older period occurred during the Triassic between the Iranian and Eurasian plates. A younger period occurred between the Arabian and Iranian plates during Late Cretaceous–Cenozoic times (Berberian & King 1981; Alavi, 1994). According to regional tectonics, palaeogeography, magmatic sequences and ophiolite remnants, two main Tethyan oceans have been identified: Palaeo-Tethys and Neo-Tethys. The first one separated the Iranian plate from Eurasia during Late Palaeozoic–Early Mesozoic time; the second one was located between the Iranian and Arabian plates during Late Mesozoic time (Stocklin, 1974). Ophiolitic remnants of these oceans have been identified in northern and SSE Iran as Palaeo- and Neo-Tethys sutures (Fig. 1a). Subduction of the Palaeo- and Neo-Tethys oceans beneath the Eurasian and Iranian plates, respectively, caused the formation of several magmatic arcs (Caucasus in the north and Sanandaj–Sirjan, Urumieh–Dokhtar and Alborz in the south). Closure of the Neo-Tethys Ocean by subduction beneath the Iranian plate (e.g. Stocklin, 1974) caused the formation of the Sanandaj–Sirjan Magmatic Zone (SSMZ), the Urumieh–Dokhtar Magmatic Arc (UDMA), the Alborz mountain belt (AMB) and the Zagros fold-and-thrust belt (ZFTB) (Fig. 1a). The detailed geological history of these linear belts is complex and some may include intra-oceanic arcs formed previously to collision and amalgamation of all the continental, microcontinental and oceanic blocks. In response to subduction, collision and post-collisional extension, extensive magmatic episodes took place in the region (Ahmadian *et al.* 2009). These include Cenozoic calc-alkaline and alkaline (potassic) magmatism and Eocene volcanics (Berberian & Berberian, 1981; H. Moinvaziri, unpub. Ph.D. thesis, Univ. Paris-Sud, Orsay, 1985) formed in arc and back-arc settings within an extensional (post-collisional) environment (Berberian, 1983; Hassanzadeh *et al.* 2002; Allen *et al.* 2003) along the AMB and UDMA.

The reconstruction of tectonic and magmatic episodes requires a precise knowledge of radiometric ages and a characterization of petrogenetic processes. However, a key point is that the precise time of collision between Arabia and Eurasia is still controversial. Age estimates for the onset of collision are varied: Late Cretaceous (Stocklin, 1974; Berberian & King, 1981; Alavi, 1994; Mohajjel & Fergusson, 2000) to Eocene (Ghasemi & Talbot, 2006; M. Aghazadeh, unpub. Ph.D. thesis, Tarbiat Modares Univ., 2009), Eocene–Oligocene (Hooper *et al.* 1994; Horton *et al.* 2008), Oligocene (Yilmaz, 1993), Miocene (Stoneley, 1981; Şengör & Natal'in, 1996; Robertson, 2000; Mohajjel, Fergusson & Sahandi, 2003; McQuarrie *et al.* 2003) and Pliocene (Philip *et al.* 1989).

According to geochemical characteristics of Eocene to Miocene magmatic rocks, Haschke *et al.* (2010) proposed a minimum age of 21 Ma for the Alpine–Himalayan onset of collision in Central Iran. Middle to Late Cenozoic magmatism in the hinterland,

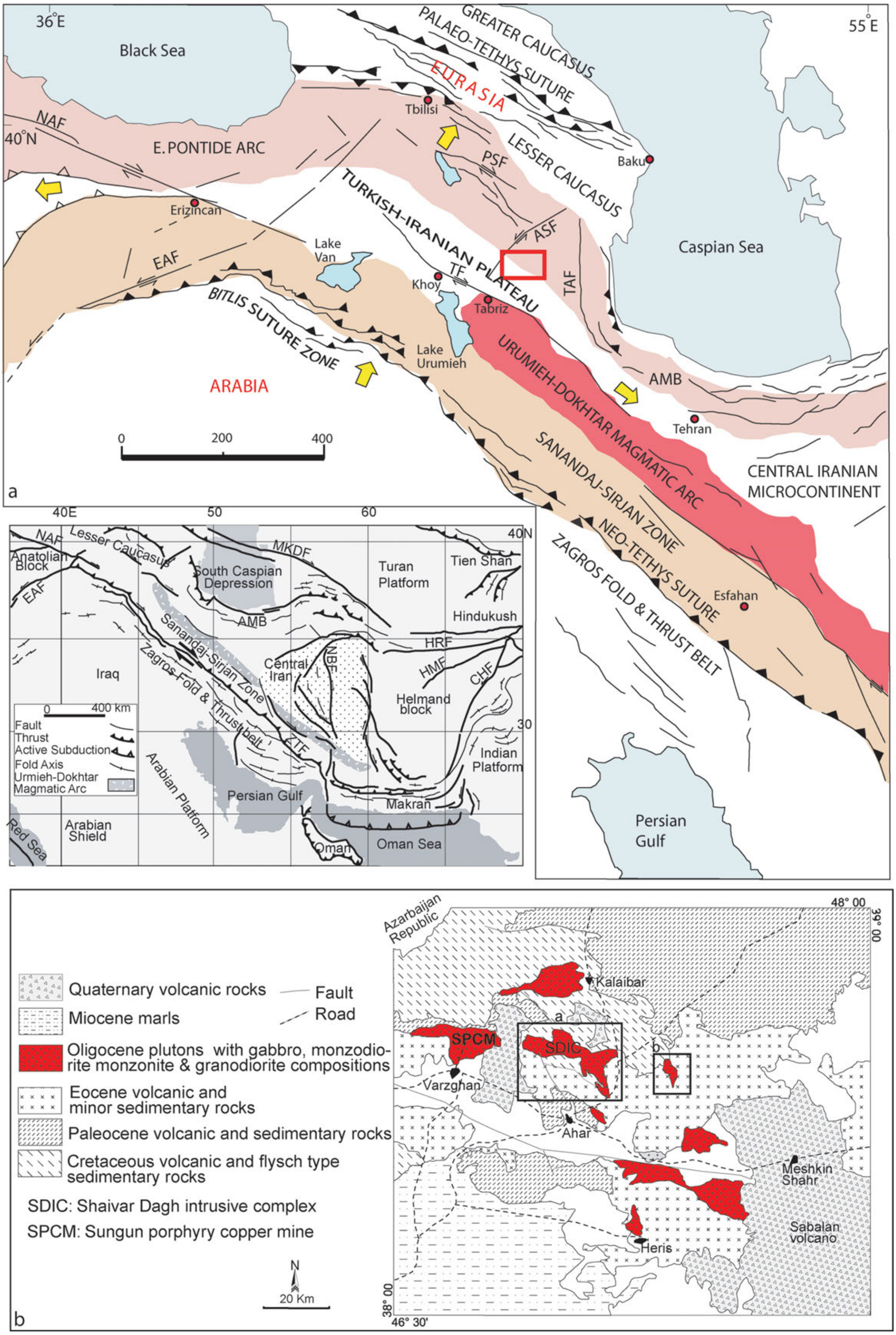

Figure 1. (Colour online) (a) Simplified tectonic map of NW Iran, eastern Turkey and the Caucasus within the Arabia–Eurasia collision zone (inset) showing the active plate boundaries and plate convergence vectors with respect to a fixed Eurasia (yellow arrows). The area is located between the great Caucasus Palaeo-Tethys suture in the NE and Zagros-Biltis Neo-Tethys suture in the SW. Position of the sutures after Dercourt *et al*. (1986). (b) Geological map of the Ahar region. Simplified and modified after Babakhani, Lesquyer & Rico (1990). Other abbreviations: AMB – Alborz Mountain Belt; EAF – East Anatolian Fault; NAF – North Anatolian Fault; ZTF – Zagros Thrust Fault; NBF – Nayband Fault; MKDF – Main Kopeh-Dagh Fault; HRF – Herat Fault; HMF – Helmand Fault; CHF – Chaman Fault; ASF – Aras Fault; PSF – Pampak–Sevan Fault; TF – Tabriz Fault; TAF – Talesh Fault.

represented by the UDMA and AMB, is attributed to a sequence of episodes starting with direct subduction (e.g. Berberian *et al.* 1982; Shahabpour, 2007, among others), slab break-off (Ghasemi & Talbot, 2006) and slab roll-back (Ahmadzadeh *et al.* 2010). Consequently, varied petrogenetic models have been suggested from continental arc settings (Berberian & King, 1981; J. Hassanzadeh, unpub. Ph.D. thesis, Univ. California, Los Angeles, 1993) to continental rifting (Amidi, Emami & Michel, 1984) and post-collisional extension (Ahmadian *et al.* 2009; M. Aghazadeh, unpub. Ph.D. thesis, Tarbiat Modares Univ., 2009).

2.a. Overview of the Tertiary magmatism of the Alborz mountain belt

The Alborz mountain belt is located north of Iran, extending for about 2000 km from the Lesser Caucasus in Armenia and Azerbaijan in the northwest to the Paropamisus Mountains of Northern Afghanistan in the east. It is formed by a composite polyorogenic belt resulting from the Cimmeride and Alpine orogenic events and shows a regional tectonic history that has largely remained uncertain. The polyorogenic AMB (Alavi, 1996) consists mainly of Upper Precambrian to Eocene sedimentary and volcanic successions. These were intruded by Mesozoic to Cenozoic plutons (Stöcklin, 1974; Annells *et al.* 1975; Berberian & Berberian, 1981) in the WNW zone of the belt. The AMB is bounded to the north and northeast by the Palaeo-Tethys suture zone, which is overprinted by the later Alpine structures. The southern boundary of the AMB is defined by the Central Iran microcontinent. In NW Iran (Azerbaijan–Arasbaran zone), the AMB is juxtaposed against the UDMA, one of the two main magmatic alignments of the Zagros orogenic belt (Fig. 1a).

Cenozoic sequences of the AMB are represented mainly by submarine and subaerial, porphyritic and non-porphyritic, massive lava flows of andesite, basaltic andesite and basalt compositions. Rhyolites, dacites and extensive well-bedded pyroclastic deposits of broadly andesitic composition complete the sequence. In the northwestern part of the AMB, Cenozoic strata were intruded by Oligo-Miocene plutons of shoshonitic and high-K calc-alkaline affinities (Berberian & Berberian, 1981; Aghazadeh *et al.* 2010). This plutonic activity is typically post-collisional, post-dating the main orogenic events in the AMB and Zagros. It sets an interesting problem about their potential relationship with earlier subduction processes. Whether magmatism resulted from subduction of Neo-Tethys oceanic crust beneath the Iranian plate, or alternatively from extension and late- to post-collision events, is a matter of ample debate. The fact that this Cenozoic magmatic belt containing calc-alkaline and shoshonitic intrusions is more than 30 Ma younger and more than 300 km further from the suture, compared to the outer and older SSMZ (Alavi, 1994, 2004; Omrani *et al.* 2008) sets an interesting problem difficult to understand in any of the currently applied, subduction-related petrogenetic models. Plausible solutions require a good knowledge of the timing between magmatism and tectonism. However, the geological history of the important magmatic arcs in the Tethyan orogenic belts in Iran (AMB, UDMA and SSMZ) is still poorly known.

Transition of the older SSMZ to the younger and more distant UDMA has been attributed to a change in subduction processes (e.g. a change in slab dip; Berberian & Berberian, 1981; Shahabpour, 2007; Omrani *et al.* 2008) and, alternatively, to the existence of two distinct subduction zones (Azizi & Moinvaziri 2009). Nevertheless, the existence of two Tertiary magmatic belts (UDMA and AMB; Fig. 1a) with abundant plutonic and volcanic rocks of calc-alkaline and potassic affinities far north from the orogenic suture of the Zagros is a major problem that will require detailed petrological and geochronological studies.

In summary, three main plutonic rock associations are recognized in the NW of Iran: (1) Mesozoic intrusions into the SSMZ and, partially, into the Palaeozoic and Precambrian rocks of the AMB; (2) Tertiary plutonic rocks of the UDMA; (3) Tertiary monzonitic intrusives exclusively of the AMB. Some Oligocene plutonic complexes (Fig. 1b) were described from the northwestern part of the AMB (e.g. Shaivar Dagh, Khankandi, Anzan, Kalaibar, Sungun, and Ordobad; Berberian & Berberian, 1981; Babakhani, Lesquyer & Rico, 1990). However, no detailed studies about genesis, tectonic setting and relationship between different plutonic cycles have been conducted in the region. Babakhani, Lesquyer & Rico (1990) reported that monzonite and syenite are main constituents of Oligocene plutons of the AMB. A detailed study of the shoshonitic and high-K calc-alkaline Khankandi pluton was reported recently (Aghazadeh *et al.* 2010). A similar petrological study of the Shaivar Dagh intrusive complex (SDIC) is presented in this paper. With these two studies, a better knowledge of the post-collisional magmatic history is accomplished for the first time in this part of the Tethyan orogenic belt in Iran.

3. Geological setting of the Shaivar Dagh intrusive complex (SDIC)

The SDIC, studied here, is located NW of the AMB, in the Arasbaran zone, about 150 km NE of Tabriz city in NW Iran (Fig. 2). The Arasbaran zone occurs in the hinterland of the Arabia–Eurasia collision zone in the broad Alpine–Himalayan orogenic belt. This zone includes Upper Cretaceous–Cenozoic plutonic and volcanic sequences that provide important clues about collision-related continental magmatism and mantle dynamics. The Arasbaran sector is bounded by three main strike-slip faults, i.e. the Aras fault in the north, the Tabriz fault in the west and southwest, and the Talesh fault in the east (Fig. 1). The movement of these main faults caused generalized extension during the Cenozoic in response to convergence and collision between the Arabian and Turkish–Iranian plateaus.

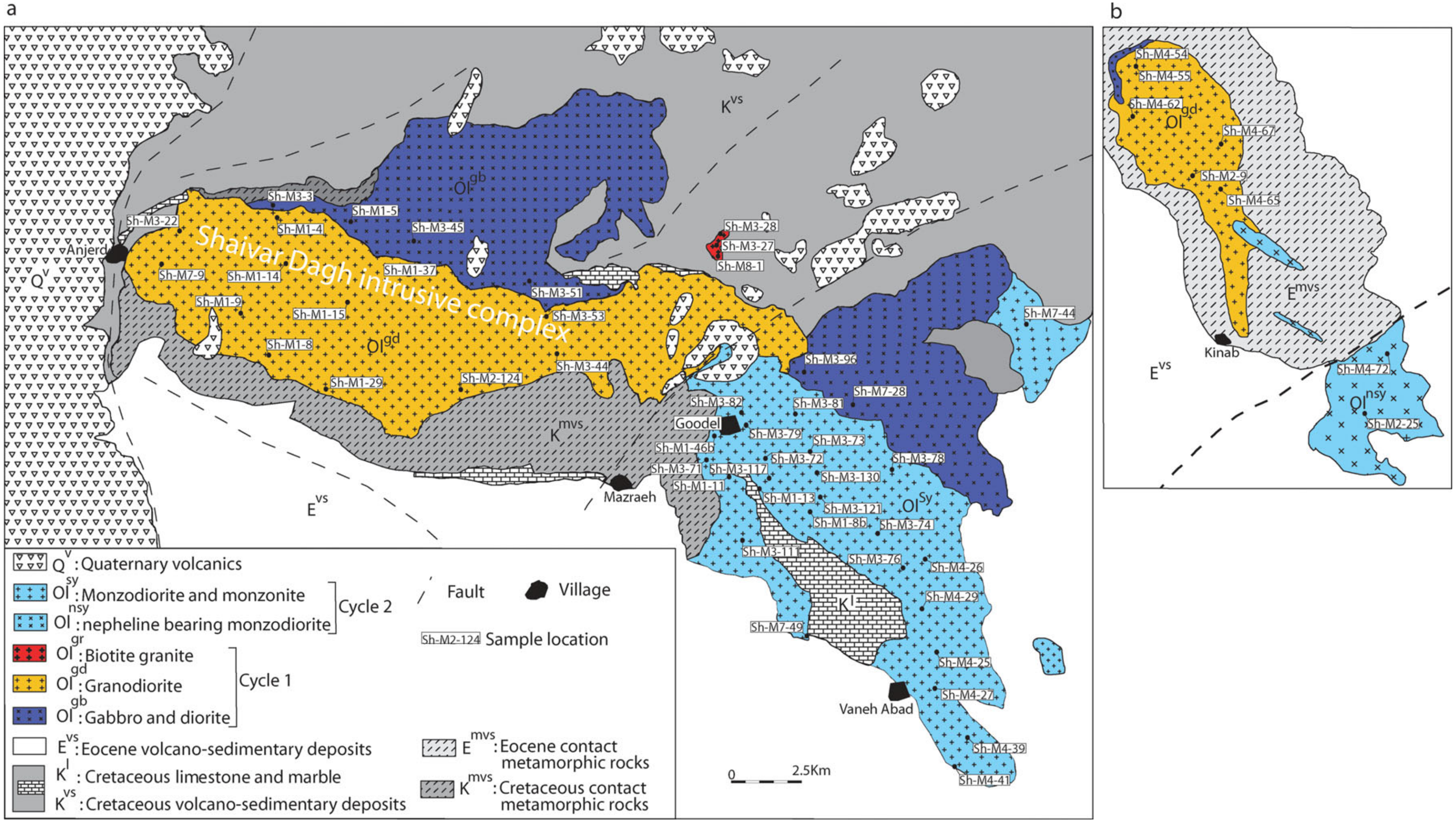

Figure 2. (Colour online) Geological map of the Shaivar Dagh intrusive complex. (a) Western and central parts. (b) Eastern part. Simplified after Aghazadeh (2006).

The activity of subduction, collision and post-collision events related to tectonic processes during the Late Mesozoic and Cenozoic periods gave rise to the most prominent geological features of the Arasbaran zone. Most parts of the Arasbaran area are covered by Upper Cretaceous and Tertiary sediments. The study of the few outcrops of Palaeozoic and Precambrian rocks that are found in the zone reveals a common geological history for both the Azerbaijan–Arasbaran and Central Iran microcontinents (Berberian & King, 1981). Precambrian lithologies include metamorphic, igneous and sedimentary rocks that are exposed along faulted and uplifted crustal blocks.

Magmatism in the area began during Late Cretaceous time and continued during the Cenozoic and Quaternary. The Upper Cretaceous–Paleocene marine volcanism includes intermediate to acidic lava flows and pyroclastic rocks with calc-alkaline to high-K calc-alkaline affinity (M. Aghazadeh, unpub. Ph.D. thesis, Tarbiat Modares Univ., 2009). This period of intense volcanic activity is associated with deep-sea marine sediments. Two main Cenozoic–Quaternary volcanic episodes are recognized. (1) An Eocene sequence consists of trachybasalts and basaltic trachyandesites with subordinate tephrite-basanite, phonolites and basaltic andesite. This sequence has mildly alkaline and shoshonitic affinities (Dilek, Imamverdiyev & Altunkaynak, 2009) and is overlain by the Upper Eocene flysch deposits and/or Upper Miocene volcanic and sedimentary sequences. (2) The second volcanic episode is formed by Upper Miocene–Quaternary rocks (ages according to stratigraphic relations) grouped into two main sequences. The earlier sequence is formed by Upper Miocene–Lower Pliocene basanite, basalt, andesite, trachyandesite, trachydacite, dacite and rhyolite lavas. The later is formed by Upper Pliocene–Quaternary trachybasalt, basaltic andesite, trachyandesite, trachyte and rhyolite flows. Upper Miocene–Pliocene volcanic sequences are accompanied by shallow sea sediments. All these volcanic rocks are characterized by high-K calc-alkaline and shoshonitic affinities (M. Aghazadeh, unpub. Ph.D. thesis, Tarbiat Modares Univ., 2009). The latest magmatic pulse in the Plio-Quaternary is represented by alkaline rocks showing within-plate geochemical signatures (Pearce, Bender & De Long, 1990; Keskin, 2003; Kheirkhah *et al.* 2009).

Cenozoic plutonic rocks with shoshonitic affinities (M. Aghazadeh, unpub. Ph.D. thesis, Tarbiat Modares Univ., 2009; Aghazadeh *et al.* 2010) are widespread throughout the Arasbaran zone and the western part of the AMB. The Cenozoic plutonism of the Arasbaran Zone can be divided into two main episodes, (1) Oligocene intrusions, and (2) Miocene intrusions, which have been considered part of the southeastern extension of Lesser Caucasus plutonism (Khain, 1977). These plutonic rocks are polycyclic in the sense that they contain more than one genetic unrelated magmatic series. According to Jahangiri (2007), the Miocene intrusive rocks display adakitic signatures and were formed in relation to slab roll-back or slab break-off in a post-collision setting. Aghazadeh *et al.* (2010) yielded a zircon U–Pb age of 28.9 Ma age for the Khankandi monzonitic pluton, which was emplaced in a post-collisional tectonic setting. The SDIC, studied in this paper, intruded into Cretaceous and Eocene volcanosedimentary successions. A detailed description of the main rock types and field relations of this intrusive complex is given here in the next Section.

4. Intrusive units and field relationships of the SDIC

The SDIC is a 40–45 km long elongated body, oriented on a NW–SE trend, cropping out to the N and NE of Ahar city (Fig. 2). The SDIC includes mafic to felsic intrusive bodies. In order to follow a systematic description, the rocks were initially classified by field and petrographic criteria based on the colour index and feldspar mineralogy. Subsequently, this provisional classification was corrected using chemical and mineralogical criteria that, in general terms, follow the QAP classification scheme. All intrusive rocks of the SDIC can be grouped into two main magmatic cycles (Fig. 3). Cycle 1 includes gabbro-diorites, massive granodiorites and associated mafic microgranular enclaves, as well as biotite granites. Cycle 2 includes massive monzodiorites and monzonites as well as mafic microgranular enclaves of broadly the same composition as the hosting rocks. These two magmatic cycles can be distinguished in the TAS classification (Fig. 3a) and MALI (modified alkali-lime index)–SiO_2 diagrams (Frost *et al.* 2001; Fig. 3b).

Lithologically and tectonically the SDIC can be divided in three zones, namely western, central and eastern (Fig. 2). Outcrops to the west of the Mazraeh skarn copper deposit and Mazraeh fault (western zone of the SDIC) mainly belongs to Cycle 1 rocks. In this zone, granodioritic outcrops are dominant. They are surrounded by gabbros and diorites that form the marginal parts of the intrusion to the north of the complex. According to field relationships and zircon age dating (see Sections 7, 8.a) the Cycle 1 rocks are the oldest intrusive units in the SDIC. Only a few outcrops of biotite granites as stocks and dykes can be found in the northern parts of the granodioritic body in the western zone (Fig. 2a). The relationships between biotite granite and other rocks are not clearly exposed but the biotite granitic dykes cut granodiorites and related gabbro-diorites. In the western zone, skarn type copper mineralizations are developed at the contact between granodiorites and the Cretaceous calcareous strata. The central zone of the SDIC contains rocks of Cycle 2 (Fig. 2a). The contact between the eastern and central zones of the SDIC is covered by Cretaceous and Eocene deposits. This eastern zone contains granodiorites, gabbro-diorites and monzodiorites. The contact between monzodiorites and granodiorites in the eastern zone is faulted but some monzodioritic dykes cross-cut the granodiorites

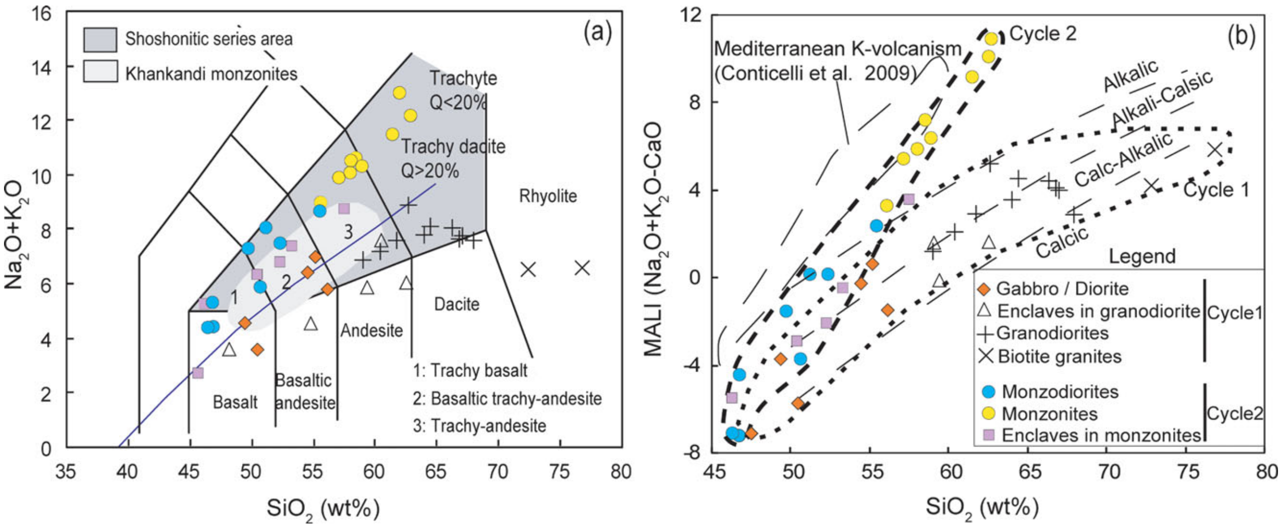

Figure 3. (Colour online) (a) Total alkalis v. silica plot with IUGS fields after Le Maitre (2002). (b) MALI–SiO_2 diagram (Frost *et al.* 2001) showing the two different magmatic cycles of the Shaivar Dagh intrusive complex. See text for explanations.

(Fig. 2b). Field relationships and zircon age data (see Sections 7, 8.a) confirm that the Cycle 2 units are the youngest intrusive bodies in the SDIC.

Gabbro-diorites (Cycle 1) are fine- to medium-grained (porphyritic) rocks. Most of them are exposed at the northern and marginal parts of the granodioritic body in the western zone. They consist of clinopyroxene, amphibole and plagioclase ± quartz ± alkali feldspar. Based on the composition of mafic minerals, these rocks can be grouped into amphibole- and clinopyroxene-rich sub-types. Fine-grained rocks contain clinopyroxene as the main mafic mineral while medium- to coarse-grained rocks show primary amphibole as the main mafic mineral. Clinopyroxene-rich outcrops are extensive in the area.

The porphyritic granodiorite pluton contains pinkish alkali feldspar megacrysts (up to 6 cm in length) in a medium- to coarse-grained matrix. The matrix is composed of alkali feldspar, biotite, amphibole and quartz ± clinopyroxene. In the marginal parts of the pluton, alkali feldspar megacrysts are orientated. Fine-grained, mafic microgranular enclaves (MME), ranging in size from 5 cm to 2 m in length, are enclosed in the granodiorites, preferentially in the marginal parts. They may show either gradual or sharp contacts with the host granodiorite. The enclaves contain dispersed K-feldspar megacrysts (1–5 cm). According to the composition of mafic minerals, enclaves can be grouped into clinopyroxene- and amphibole-rich sub-types. In addition to fine-grained mafic enclaves (MME type), some mafic bodies with an autolithic nature and porphyritic texture can be found, especially in the marginal parts of the granodiorite.

Cycle 2 intrusive rocks include monzonites and associated monzodiorites, which may show either gradual or intrusive relations. Monzodiorites are also represented in dykes and stocks in the area. Field relations show that monzonites form small intrusions or magma pulses into previously emplaced monzodioritic magma. Monzodiorites are fine- to medium-grained rocks, often with isotropic fabrics. Clinopyroxene, amphibole, biotite, plagioclase and K-feldspar are the main constituents. Some gabbroic facies appear in the eastern zone where they may contain nepheline, olivine and brown amphibole.

Monzonites are meso- to leucocratic, medium- to coarse-grained rocks. The size of feldspar and pyroxene crystals reaches up to 1 cm. These rocks show porphyritic and fine- to medium-grained textures in patches in the SE part of the central zone. They are composed of clinopyroxene, amphibole, biotite, plagioclase, K-feldspar ± feldspathoid ± quartz. Some feldspathoid-bearing rocks locally appear in the western parts of the central zone. Pyroxenitic patches showing gradual contacts with the host monzodiorite are locally observed in the marginal parts. Massive monzonites form the larger volumes of the SDIC in the central zone. They host fine-grained mafic magmatic enclaves (5–20 cm length) that may range in composition from monzogabbro to monzodiorite. Most of these show chilled margins and sharp contacts with the host monzonite. Monzodiorite patches with a 10–100 m size also can be found within the massive monzonites, especially in the marginal parts of the stocks. Pegmatitic monzonites appear in dykes and apophyses intruded into both the Cretaceous country rocks and the marginal monzodiorites. These are composed of euhedral alkali feldspar megacrysts, up to 10 cm in length, in a coarse-grained leucocratic matrix.

Country rocks are Cretaceous and Eocene deposits. Submarine Cretaceous deposits are mainly volcanic and volcaniclastic rocks with intercalations of deep-sea sediments. Volcanic rocks include basalt, andesitic basalt, andesite and dacite. The Cretaceous deposits are metamorphosed near the contact with the SDIC units. The grade of metamorphism is locally high, at pyroxene hornfels facies, especially near the Cycle

2 units in the central zone. The Eocene volcanic rocks include trachybasalt, trachyandesite, andesite, trachyte, tephrite, dacite and volcaniclastic rocks. Near the SDIC, they have undergone regional argillic, silicic and propylitic alterations. The Eocene deposits in the metamorphic aureole are metamorphosed at amphibole-hornfels facies, especially in the western and eastern zones of the SDIC. The Quaternary trachybasalts and trachyandesites are the last episode of magmatism in the region and they overlie all the older rocks.

5. Petrography and mineral compositions

Rocks of the two magmatic cycles show marked differences in textures and mineral assemblages. Here, petrographic and mineralogical characteristics of the main rock types distinguished in the SDIC are described in detail. Mineral compositions and classification diagrams are given in the online Appendix 1 at http://www.journals.cambridge.org/geo.

5.a. Gabbro-diorites (Cycle 1)

Gabbro-diorites are fine- to medium-grained porphyritic rocks. Phenocrysts are mainly plagioclase and rarely clinopyroxene and amphibole. The compositional range of these rocks varies from gabbro and diorite to quartz diorite and quartz monzodiorite. According to the composition of mafic minerals, they can be grouped into amphibole-rich and pyroxene-rich sub-types. In the clinopyroxene-rich sub-type, clinopyroxene and biotite are the main mafic minerals. Euhedral to subhedral clinopyroxene have salite composition ($Wo_{44-46}En_{39-42}Fs_{11-13}$). They contain low Al_2O_3 (0.8–2.1 %) and TiO_2 (0.1–0.3 %), and have high Mg nos. (0.65–0.68). Biotites show high Mg nos. (0.59–0.60), TiO_2 (3.5–4 %) and plot into the high-Mg biotite field. In the amphibole-rich sub-type, green amphiboles range in composition from magnesio-hornblende to actinolite. They have high Mg nos. (0.70–0.81) and low TiO_2 (0.9–1.26 %), Al_2O_3 (5.5–6.2 %) and total alkalis (1.2–2.2 %). Some amphiboles contain clinopyroxene inclusions. Plagioclase shows a wide range in composition (An_5 to An_{55}) in both sub-types. Quartz and alkali feldspar are interstitial phases in the diorite facies.

5.b. Granodiorites (Cycle 1)

Granodiorites are coarse-grained leucocratic to mesocratic rocks that contain K-feldspar megacrysts (1–6 cm length). Tonalite and quartz-monzonite facies appear locally associated. In the central parts, amphibole is the dominant mafic mineral but in the marginal zones, clinopyroxene is abundant and partially replaced by green amphibole. Magnesio-hornblende is the main amphibole, although minor actinolite and edenite are present. Actinolitic amphiboles mostly appear at the rims of large amphibole crystals. Amphiboles contain high Mg nos. (0.69–0.72), low TiO_2 (0.2–1.3 %) and total alkalis (0.7–2.1 %). The content of FeO and SiO_2 in the amphiboles increases from the core to the rims of the crystals and the content of MgO, Al_2O_3 and TiO_2 decreases. In the central parts of the pluton, amphiboles have low Al_2O_3 contents (3–6 %) in comparison with amphiboles of the marginal zones (5–7 %).

Clinopyroxene is found as relict inclusions inside amphiboles and alkali feldspar megacrysts in the margins of the granodiorite. They have salitic composition ($Wo_{45}En_{41}Fs_{13}$), low TiO_2 (0.3 %), Al_2O_3 (1.8 %) and high Mg no. (0.87) and Cr (0.6 %). Micas are brown to greenish brown with high Mg nos. (0.62–0.66), variable and high TiO_2 (0.01–5 %) and F (0.3–1.5 %). Some biotite crystals are surrounded by amphibole. Plagioclase appears as euhedral to subhedral crystals showing a marked compositional zoning from andesine to oligoclase. Two types of alkali feldspar are distinguished in the granodiorite. One is formed by euhedral megacrysts and the other by anhedral crystals, which are associated with quartz forming poikilitic and interstitial aggregates.

According to the mineralogy, enclaves in the granodiorites can be divided into two types: clinopyroxene-rich and amphibole-rich. Medium-grained, clinopyroxene-rich enclaves are included in the marginal parts of the granodiorite massif. Fine- to medium-grained, amphibole-rich, mafic microgranular enclaves can be found in the central parts. Clinopyroxene-rich types have monzogabbroic composition but amphibole-rich types have diorite, quartz-diorite and quartz-monzodiorite composition. Porphyritic, microgranular and granular textures are common in the clinopyroxene-rich enclaves. The main mafic minerals are clinopyroxene and biotite, which are associated with green amphiboles that partially replaced clinopyroxenes. Clinopyroxene composition ranges from salite to high-Ca augite ($Wo_{43-48}En_{25-45}Fs_{11-24}$). They show variable MgO (9–16 %), FeO (7–15 %), Al_2O_3 (1–3 %) and CaO (21–24 %) contents. Amphiboles are high Mg no. (0.8–0.85) magnesio-hornblende. Biotites also have high Mg nos. (0.61–0.63) and high TiO_2 (4–4.5%) contents. Plagioclases show compositional zoning from An_{77} to An_{24}.

Amphibole-rich enclaves show porphyritic and granular textures in most cases. They are composed of amphibole, biotite and plagioclase. Some quartz and alkali feldspars can be found in the enclaves. Relicts of clinopyroxene crystals are rarely present in the cores of amphibole crystals. Amphiboles are classified as magnesio-hornblende with Mg no. ranging from 0.70 to 0.75. Similar to biotites in the clinopyroxene-rich enclaves, biotites of these enclaves contain high Mg nos. ($X_{Mg} = 0.60–0.65$) and high TiO_2 contents (3–3.5 %). Plagioclases have variable anorthite contents from An_{48} to An_{12}.

Biotite granites show medium- to coarse-grained textures with biotite as the main mafic mineral. Additionally, they have garnet and varied accessory minerals (allanite, zircon and titanite). Biotites are richer in iron (Mg no. = 0.41–0.43) compared to the granodiorite biotites. Plagioclase forms euhedral to subhedral crystals that show a compositional zoning from An_{34} to An_{21}.

5.c. Monzodiorites and monzonites (Cycle 2)

Monzodiorites and monzonites show varied textures and mineralogy. The monzodiorites are medium- to coarse-grained, mesocratic to melanocratic, porphyritic rocks with clinopyroxene, amphibole and mica as mafic minerals (up to 60 vol. %). Modal contents of mica, clinopyroxene and K-feldspar are extremely variable in the monzodiorites. Towards the marginal parts, some mafic patches showing abundant mica and clinopyroxene can be found. These may have up to 80–90 vol. % of clinopyroxene. Towards the more monzonitic (less mafic) masses, modal content of K-feldspar and amphibole increases and the relative proportion of clinopyroxene and plagioclase decreases. Anhedral alkali feldspar can be often found at the interstices between other minerals. However, in some areas they may appear as phenocrysts. Clinopyroxene forms euhedral to subhedral zoned crystals of dominantly salitic composition. Towards the margins, the amount of MgO, Al_2O_3, TiO_2 and Na_2O decreases and SiO_2, FeO and CaO increases. Clinopyroxenes contain 2.5–4 % Al_2O_3, 0.53–0.68 Mg no., 0.3–1 % Na_2O and less than 0.6 % TiO_2. In the nepheline-bearing monzodiorites, clinopyroxene crystals may contain high TiO_2 (>0.8 %), Na_2O (>0.8 %) and Al_2O_3 (3.5–6 %). Amphiboles in the monzodiorites are brown magnesio-hastingsites, but rare green actinolite can also be found. Brown amphiboles are partially replacing clinopyroxenes. They contain low and variable Mg nos. (0.45–0.65) and high TiO_2 (2–3 %) and total alkali (3–5 %) contents. Mica plots in the high-Mg biotite field (Mg no. = 0.5–0.65) and shows high and variable TiO_2 contents (2–5 %). In the nepheline-bearing monzodiorites, micas have phlogopitic composition (Mg no. = 0.7–0.8) and high TiO_2 (6–6.5 %) and F (0.8–1.6 %) contents. Plagioclases show variable compositions from An_{13} to An_{82} and marked compositional zoning (An_{54} to An_{25}). Anhedral alkali feldspar is perthitic and includes hypersolvus cores (Ab_{9-67}–Or_{21-89}).

In the nepheline-bearing monzodiorites, plagioclase crystals have high anorthite contents (An > 45 %) and high orthoclase molar proportions (up to 9 %). The alkali feldspar is hypersolvus (Ab_{8-65}–Or_{31-89}). In addition to common mafic minerals that are present in the monzodiorites, olivine and nepheline can be found (nepheline-bearing monzodiorites). Olivines (Fo = 72–73 %) are surrounded by clinopyroxene and brown amphibole forming a coronitic texture. Anhedral nepheline crystals are replaced partially or completely by zeolites.

Monzonites are equigranular, mesocratic, fine- to coarse-grained porphyritic rocks with locally pegmatitic facies. The composition varies from nepheline-monzonite, monzonite to quartz-monzonite. Clinopyroxene, amphibole and mica are the dominant mafic minerals (<30 vol. %). Euhedral to subhedral clinopyroxenes are salitic. However, in the pegmatitic facies, clinopyroxenes are richer in alkalis and have aegirine augite compositions. The amount of Na_2O in the clinopyroxenes (0.6–2 %) of the nepheline-bearing monzonites is higher with respect to the clinopyroxenes of monzonites (0.3–0.7 %). Pegmatitic clinopyroxenes have the highest Na_2O contents (0.8–6 %) and the lowest Mg nos. (0.3–0.5). Clinopyroxene crystals in the monzonites include abundant inclusions of opaque minerals and apatite. In the monzonites, clinopyroxene is partially replaced by amphibole and biotite. It contains 1–4 wt % Al_2O_3 and less than 1 wt % TiO_2. In these crystals, the amount of MgO and SiO_2 decreases towards the margins and the amount of TiO_2, FeO, Al_2O_3 and alkalis increases. Amphiboles in the monzonites are brown and show magnesio-hastingsite and hastingsite composition. Magnesio-hornblende and actinolite are locally developed surrounding clinopyroxenes and brown amphiboles. Green-brown mica crystals have biotite to high-Mg biotite compositions (Mg no. = 0.45–0.65) and they contain low TiO_2 (1–1.5 wt %). Euhedral to subhedral plagioclases show compositional zoning with albitic margins. They show oligoclase composition, although towards monzodiorites the central parts of these crystals contain higher anorthite content. Anhedral alkali feldspars are perthitic and partially hypersolvus in the central parts. In most cases, feldspatoids have been replaced by secondary minerals (e.g. zeolites). K-syenitic pegmatites are composed of nepheline and garnet. Garnet shows andraditic composition; however, large crystals in the central parts are melanite and have $TiO_2 > 1$ wt %. Amphiboles have edenitic composition in the monzonitic pegmatites.

Enclaves in the monzonites show monzodioritic to dioritic compositions. They are composed of large amount of amphibole crystals, clinopyroxene and biotite. Compositionally, clinopyroxenes and biotites are comparable to those of the massive monzonite and monzodiorite. Amphiboles are green (hornblende and actinolite) and brown (Mg-hastingsite).

6. Whole-rock geochemistry

6.a. Sampling and analytical techniques

About 200 samples were collected from magmatic rocks of the SDIC. A set of 51 fresh, unaltered samples was selected for major and trace element analyses. Sample location and mineral modes are given in online Appendix 2 at http://journals.cambridge.org/geo. Criteria for sampling were two fold; on the one hand we aimed to collect a sample set representative of all rock types in the intrusive complex. On the other hand, local variations, marginal zones and enclaves were sampled with the aim of studying possible petrogenetic

Table 1. Representative whole-rock analyses of the Shaivar Dagh intrusive complex

Rock Type[a]	Mdi	Mdi	Mdi	Mdi	Mdi	Mdi	Mdi	Mdi	Emz	Emz	Emz	Emz	Emz	Emz	Mz	Mz	Mz	Mz	Mz	Mz	Mz	Mz	Mz	Pmz	Gbd	Gbd
Sample no.	Sh-M4–72	Sh-M2–25	Sh-M4–29	Sh-M3–121	Sh-M3–130	Sh-M7–44	Sh-M1–8b	Sh-M1–46b	Sh-M3–79	Sh-M3–81	Sh-M4–26	Sh-M3–82	Sh-M3–117	Sh-M4–39	Sh-M3–71	Sh-M3–72	Sh-M3–73	Sh-M3–74	Sh-M3–76	Sh-M3–78	Sh-M3–111	Sh-M4–25	Sh-M4–27	Sh-M1–13	Sh-M3–45	Sh-M3–3
SiO_2	46.42	46.76	46.73	49.71	50.62	51.18	52.35	55.41	45.48	46.21	50.33	52.20	53.20	57.41	55.50	57.00	57.89	58.00	58.30	58.80	–	61.44	62.80	61.91	49.37	50.40
TiO_2	1.29	1.12	1.27	1.14	1.18	1.02	0.86	0.90	1.59	1.36	0.99	0.91	0.87	0.74	0.85	0.67	0.73	0.61	0.55	0.59	–	0.45	0.50	0.48	1.03	2.13
Al_2O_3	18.74	19.8	18.09	19.13	17.84	19.15	19.76	18.08	15.71	17.66	20.05	17.00	18.55	17.86	17.60	18.15	18.54	18.65	18.40	18.55	–	18.54	18.15	17.98	14.84	16.46
$Fe_2O_3{}^t$	11.45	11.44	12.16	8.42	10.48	7.63	7.03	7.36	12.96	11.37	8.39	7.90	7.75	6.24	6.57	5.78	5.28	5.09	4.49	4.69	–	3.59	2.59	1.63	11.17	13.09
MgO	3.88	3.20	3.65	2.87	3.06	2.36	2.13	2.36	6.84	4.35	2.76	4.73	2.96	1.93	2.75	2.04	1.39	1.60	1.30	1.65	–	0.56	0.33	0.58	10.29	4.04
MnO	0.19	0.15	0.20	0.16	0.20	0.17	0.14	0.16	0.21	0.18	0.13	0.15	0.17	0.12	0.15	0.15	0.14	0.15	0.14	0.14	–	0.11	0.09	0.06	0.36	0.24
CaO	11.51	9.71	11.63	8.83	9.57	7.82	7.34	6.19	13.00	10.66	9.20	8.81	7.89	5.12	5.57	4.49	4.14	3.71	3.22	4.05	–	2.33	1.40	2.90	8.24	9.27
Na_2O	2.43	2.53	2.64	3.52	2.98	3.79	3.28	3.34	1.66	2.13	2.59	3.41	3.58	3.42	3.88	4.32	3.75	4.72	4.64	4.66	–	3.84	4.47	3.12	2.02	2.89
K_2O	1.92	2.73	1.72	3.76	2.86	4.19	4.18	5.22	1.14	3.2	3.82	3.43	3.89	5.4	5.09	5.52	6.40	5.79	6.01	5.68	–	7.64	7.70	9.85	2.51	0.61
P_2O_5	0.93	0.84	0.99	0.64	0.72	0.58	0.50	0.51	1.42	1.25	0.70	0.60	0.63	0.43	0.56	0.37	0.30	0.35	0.26	0.31	–	0.15	0.06	0.13	0.18	0.42
LOI	0.86	0.99	0.63	1.04	0.37	1.35	1.73	0.50	1.33	0.76	0.58	0.50	0.39	0.60	1.17	1.20	0.76	1.19	1.18	0.30	–	0.55	0.99	1.03	0.77	0.58
Total	99.61	99.28	99.71	99.23	99.89	99.23	99.31	100.03	101.33	99.14	99.54	100.00	100.00	99.27	100.00	100.00	99.33	100.00	98.90	99.70	–	99.20	99.20	99.67	100.77	100.14
ppm																										
Sc	29.1	29.5	15.7	14.4	20.0	11.9	16.7	5.72	23.4	26.2	19.1	nd	nd	13.6	nd	nd	11.71	nd	32.94	nd	7.31	7.54	nd	1.22	38.2	39.12
V	242	276	246	152	199	153	174	158	304	227	185	197	201	126	179	124	10	103	70	103	136	76.1	47	33.8	238	250
Cr	51.4	38.2	24.8	32.4	5.02	39.1	4.31	46.5	44.3	66.4	5.98	120.0	40.0	40.4	70.0	350.0	4.4	110.0	1030.0	40.0	51.1	79.9	120.0	44.2	535.0	42.8
Co	38.1	72.5	29.3	20.9	25.1	18.3	23.0	17.1	36.5	37.0	26.2	27.6	20.1	17.9	18.1	12.0	10.37	9.4	7.2	9.7	13.1	5.73	3.4	2.35	36.7	30.7
Ni	8.07	8.41	7.78	6.38	4.54	5.61	3.36	5.45	8.44	13.5	3.22	30	5.0	6.8	6.0	5.0	1.3	5.0	6.0	5.0	0.01	1.15	4.0	4.61	199.0	10.8
Cu	82.6	610	143	96.2	87.8	61.9	78.8	79.1	80.8	163	77.5	104	42.0	67.16	58.0	49.0	35.15	32.0	17.0	39.0	49.1	25.2	15.0	0.01	0.11	33.4
Zn	100.0	168.0	112.0	81.1	83.9	69.1	80.5	83.3	96.0	100.0	62.8	82.0	89.0	44.2	81.0	80.0	68.8	81.0	81.0	75.0	61.8	78.9	65.0	39.3	258.0	63.9
Ga	56.6	72.4	37.5	39.1	45.9	37.6	56.1	40.4	38.3	43.8	47.2	19.9	21.3	55.7	20.2	19.3	41.6	19.7	20	20.8	39.7	35.5	18.2	51.7	24.5	21.9
As	1.52	6.39	1.84	6.24	2.13	6.71	3.13	4.15	2.46	3.74	2.91	nd	nd	1.50	nd	nd	5.93	nd	6.04	nd	2.53	5.55	nd	10.30	2.51	1.15
Rb	62.3	121.0	51.4	91.5	71.9	99.3	120.8	89.1	30.1	106.0	102.0	109.0	94.3	119.0	139.0	141.5	131.4	163.0	165.0	172.0	82.9	179.0	217.0	172.0	68.4	13.7
Sr	1965	2175	1794	1212	1113	1031	1746	1019	1837	1316	1516	1390	1415	967	1080	935	683	859	945	881	871	445	368	448	199	275
Y	29.5	32.9	22.5	26.9	30.8	26.2	24.5	16.1	25.4	38.5	22.3	22.7	23.2	21.6	23.5	22.4	28.9	24.6	22.5	25.2	17.1	28.9	37.2	10.1	15.5	31.3
Zr	165	118	39.6	196	122	222	178	126	47.8	106.6	94.3	155	171	94.1	185	217	237	337	295	374	104	134	805	187	11.7	68.3
Nb	13.3	25.3	6.82	36.3	18.4	34.3	29.9	17.5	5.41	27.3	23.7	24.0	12.3	28.1	22.7	25.5	48.1	37.4	33.4	40.0	14.4	41.3	53.8	49.7	3.23	15.4
Cd	0.36	0.80	0.27	0.21	0.43	0.34	0.25	0.21	0.44	0.22	0.30	nd	nd	0.20	nd	nd	0.24	nd	0.33	nd	0.54	0.47	nd	0.26	0.66	0.31
Cs	1.63	4.30	0.77	3.31	1.70	3.65	3.81	0.84	1.05	5.22	3.51	1.94	0.92	2.58	1.68	1.74	4.49	2.81	3.78	3.57	0.95	5.15	3.31	3.8	3.86	0.54
Ba	955	1057	903	685	930	632	950	1048	748	786	794	1140	1360	1009	1305	1180	710	1110	1305	1085	911	505	364	1540	360	155
La	60.4	70.9	52.6	75.4	63.1	74.5	65.4	56.4	46.7	74.8	54.2	59.4	66.6	62.6	66.0	66.0	67.3	72.4	67.8	72.5	48.5	63.8	70.2	30.4	10.2	18.4
Ce	133	152	98.8	153	133	152	132	100	111	156	115	108	110	124	118	116	140	127	118	126	99.9	134	153	64.7	25.2	51.1
Pr	16.9	18.9	14.2	19.2	16.4	18.1	15.5	13.4	14.2	21.9	12.9	12.2	12.5	13.4	13.3	12.8	16.7	13.8	12.8	13.7	10.8	16.5	19.4	8.37	2.89	5.73
Nd	63.8	68.7	55.4	64.7	57.7	60.5	52.8	47.6	59.2	75.7	44.7	46.8	49.2	42.5	49.5	47.6	52.1	50.2	45.5	48.5	39.3	53.2	75	28.9	12.4	23.5
Sm	11.3	12.1	10.0	11.1	10.4	10.3	8.79	8.14	11.3	14.1	7.63	8.48	8.87	6.88	8.55	8.02	9.08	8.29	7.41	8.12	6.96	9.38	14	4.94	2.98	5.41
Eu	3.66	3.93	3.04	3.39	3.02	3.05	2.83	2.34	3.19	3.79	2.38	2.36	2.42	2.12	2.46	2.35	2.34	2.16	2.26	2.1	2.06	2.42	2.45	1.36	1.10	1.74
Gd	9.69	10.2	8.08	8.79	8.86	8.33	7.06	6.18	9.46	12.1	6.42	8.09	8.14	5.82	8.26	7.6	7.29	7.84	7.24	8.02	5.45	7.41	12.5	3.86	3.19	6.07
Tb	1.28	1.36	1.09	1.14	1.22	1.09	0.96	0.85	1.22	1.62	0.87	0.99	1.04	0.77	1.04	0.95	1.02	1.01	0.93	1.03	0.75	1.08	1.65	0.55	0.53	1.07
Dy	5.98	6.43	5.61	5.13	5.82	5.09	4.73	4.43	6.08	7.77	4.12	4.58	4.63	3.89	4.74	4.42	5.25	4.83	4.27	4.8	3.86	5.35	7.95	2.89	3.35	5.86
Ho	1.20	1.32	0.98	1.02	1.22	1.03	0.92	0.82	1.09	1.56	0.85	0.82	0.86	0.82	0.86	0.83	1.10	0.89	0.84	0.92	0.69	1.12	1.42	0.52	0.65	1.38
Er	2.88	3.33	2.24	2.47	3.02	2.52	2.20	2.03	2.59	3.76	2.17	2.47	2.49	2.06	2.57	2.5	3.02	2.73	2.48	2.77	1.80	2.84	4.17	1.27	1.73	3.57
Tm	0.39	0.42	0.29	0.33	0.4	0.33	0.30	0.28	0.35	0.52	0.29	0.31	0.30	0.28	0.32	0.3	0.45	0.36	0.33	0.37	0.25	0.41	0.53	0.18	0.24	0.51
Yb	2.22	2.39	1.81	1.99	2.38	2.12	1.68	1.76	1.85	2.88	1.66	2.06	1.95	1.73	2.15	2.09	2.62	2.37	2.19	2.61	1.54	2.46	3.44	1.16	1.47	3.00
Lu	0.32	0.34	0.25	0.3	0.34	0.31	0.22	0.26	0.29	0.41	0.24	0.31	0.29	0.25	0.31	0.32	0.38	0.36	0.33	0.39	0.23	0.34	0.47	0.15	0.23	0.47
Ta	1.07	1.87	2.98	3.11	1.28	2.35	2.40	1.10	0.53	2.13	1.40	1.30	0.50	4.63	1.00	1.3	3.73	2.00	1.70	2.00	0.92	3.87	5.00	6.04	0.55	3.00
W	3.24	4.96	0.31	3.42	1.14	7.19	4.68	0.01	1.67	5.74	2.03	3.00	3.00	6.18	4.00	5.00	2.85	4.00	5.00	5.00	2.89	9.66	7.00	2.70	2.15	0.72
Pb	7.14	56.9	11.4	15.6	10.3	14.6	20.7	19.6	2.24	10.2	16.6	18.00	17.00	8.81	20.0	22.0	24.1	27.0	27.0	27.0	14.5	32.7	36.0	46.3	13.1	6.49
Th	4.82	16.6	6.03	23.9	9.76	22.3	16.7	13.3	2.90	8.47	14.1	16.8	3.55	16.1	8.71	10.1	36.7	19.7	19.7	21.2	8.73	36.0	20.5	15.5	1.55	1.87
U	1.40	4.40	1.77	7.69	2.54	7.20	5.21	5.22	0.50	2.64	4.37	3.74	0.89	3.64	2.31	2.68	12.6	5.72	5.46	5.75	2.55	7.94	5.32	6.62	0.44	0.64
Hf	5.18	3.47	1.57	5.34	3.63	5.69	5.24	3.92	1.70	3.45	2.89	3.70	3.70	2.78	4.30	4.70	8.45	7.00	6.00	7.70	2.94	4.37	14.2	5.79	0.56	2.26
Sum REE	313	352	254	348	307	339	296	245	269	377	254	256	269	267	278	271	308	294	272	291	222	301	366	149	66.3	127
A/CNK	0.69	0.80	0.66	0.74	0.70	0.77	0.85	0.81	0.57	0.67	0.80	0.67	0.76	0.86	0.80	0.85	0.90	0.90	0.92	0.87	–	0.98	0.99	0.85	0.70	0.74
K_2O/Na_2O	0.79	1.08	0.65	1.07	0.96	1.11	1.28	1.56	0.69	1.50	1.47	1.01	1.09	1.58	1.31	1.28	1.71	1.23	1.30	1.22	–	1.99	1.72	3.16	1.24	0.21
Total alkali	4.34	5.26	4.35	7.28	5.85	7.97	7.46	8.56	2.80	5.33	6.40	6.84	7.47	8.82	8.97	9.84	10.15	10.50	10.60	10.30	–	11.48	12.17	12.97	4.52	3.50
Mg no.[b]	0.40	0.36	0.38	0.41	0.37	0.38	0.38	0.39	0.51	0.43	0.40	0.54	0.43	0.38	0.46	0.41	0.35	0.39	0.37	0.41	–	0.24	0.20	0.42	0.65	0.38
Eu/Eu*[c]	1.07	1.09	1.04	1.05	0.97	1.01	1.10	1.01	0.95	0.89	1.05	0.88	0.88	1.03	0.90	0.93	0.89	0.82	0.95	0.80	1.03	0.89	0.57	0.96	1.09	0.93
La_n/Yb_n	18.2	19.8	19.4	25.3	17.7	23.4	26.1	21.4	16.9	17.3	21.8	19.2	22.8	24.1	20.5	21.1	17.1	20.4	20.7	18.5	21.1	17.3	13.6	17.5	4.63	4.12

Table 1. (continued)

Rock type	Gbd	Gbd	Gbd	Gbd	EGd	Egd	Egd	Egd	Egd	Egd	Egd	Gd	Gd	Gd	Gd	Gd	Gd	Gd	Gd	Gd	Gd	Gd	Bgr	Bgr	Bgr
Sample no.	Sh-M7–28	Sh-M1–5	Sh-M3–51	Sh-M3–96	Sh-M4–62	Sh-M4–54	Sh-M3–22	Sh-M1–14	Sh-M1–8	Sh-M4–65	Sh-M4–67	Sh-M2–9	Sh-M1–29	Sh-M1–9	Sh-M1–15	Sh-M1–4	Sh-M1–37	Sh-M4–55	Sh-M3–53	Sh-M3–44	Sh-M7–9	Sh-M2–124	Sh-M3–28	Sh-M3–27	Sh-M8–1
SiO_2	–	55.10	54.45	56.14	48.37	54.68	–	58.98	59.32	–	62.46	59.07	60.40	61.70	62.64	64.01	64.45	66.33	66.98	66.73	67.94	–	–	72.68	76.80
TiO_2	–	1.16	1.20	0.99	0.76	0.60	–	0.93	0.95	–	0.75	0.82	0.83	0.72	0.60	0.58	0.60	0.51	0.48	0.50	0.47	–	–	0.33	0.28
Al_2O_3	–	18.04	17.86	16.38	14.53	17.03	–	16.02	14.40	–	15.72	17.46	16.56	16.45	16.00	16.31	16.00	15.44	15.87	15.83	15.34	–	–	13.51	12.05
$Fe_2O_3^t$	–	7.02	8.09	7.86	11.80	4.71	–	7.11	5.91	–	5.35	5.86	5.56	5.16	5.21	4.55	4.16	3.46	3.30	3.55	0.89	–	–	2.76	2.77
MgO	–	2.75	2.99	3.17	5.37	5.51	–	2.48	5.28	–	2.66	2.21	2.07	1.92	1.54	1.18	1.54	1.37	1.12	1.43	1.36	–	–	0.69	0.55
MnO	–	0.10	0.13	0.19	0.20	0.10	–	0.17	0.15	–	0.09	0.08	0.07	0.09	0.06	0.08	0.08	0.06	0.07	0.05	0.03	–	–	0.04	0.05
CaO	–	6.36	6.66	7.25	14.00	12.44	–	5.64	6.01	–	4.34	5.66	5.14	4.66	3.70	4.27	3.56	3.58	3.61	3.49	4.72	–	–	2.18	0.72
Na_2O	–	3.82	3.44	3.49	2.12	3.98	–	3.59	5.02	–	4.32	3.78	3.69	3.61	3.39	3.28	3.51	3.45	3.53	3.60	3.74	–	–	2.69	3.73
K_2O	–	3.15	2.93	2.26	1.39	0.49	–	3.47	0.79	–	1.58	3.09	3.48	3.93	5.46	4.53	4.57	4.54	4.13	4.01	3.87	–	–	3.68	2.83
P_2O_5	–	0.57	0.55	0.50	0.48	0.45	–	0.38	0.60	–	0.26	0.40	0.36	0.29	0.25	0.23	0.27	0.22	0.18	0.20	0.19	–	–	0.08	0.04
LOI	–	1.34	0.83	1.26	0.41	0.60	–	1.27	–	1.84	0.81	0.93	0.59	0.48	0.80	0.50	0.61	0.61	0.63	0.72	–	–	0.87	0.68	
Total	–	99.41	99.15	99.49	99.44	100.60	–	100.04	98.43	–	99.39	99.24	99.10	99.13	99.33	99.82	99.24	99.57	99.89	100.03	99.27	–	–	99.53	100.50
ppm																									
Sc	12.50	11.20	20.80	8.90	38.60	15.20	16.50	16.10	9.09	10.90	2.42	4.41	13.40	4.10	1.65	9.72	3.59	1.76	8.83	8.73	7.10	8.63	1.79	7.89	nd
V	150.6	95.7	168	108	231	122	140	149	133	106	65.9	103	137.	101	61.7	85.1	62.9	50.7	73.5	71.8	59.9	105.4	30.2	37.3	5.0
Cr	133.4	5.49	21.1	39.7	116	103	384	60.3	91.2	165.0	57.7	49.0	30.6	87.7	39.5	88.8	68.4	70.8	92.6	147.0	82.6	101.0	263.0	8.06	110.0
Co	24.4	9.96	34.3	10	41.3	15.2	28.0	17.5	18.9	16.1	10.4	13.6	19.7	13.2	6.84	7.96	8.69	6.87	3.10	10.40	2.44	13.30	3.75	5.63	2.10
Ni	77.1	2.34	23.6	4.45	33.0	42.9	168.0	6.32	40.7	57.9	13.69	15.9	20.7	14.7	8.33	5.53	11.5	10.7	13.9	18.9	14.5	13.2	3.22	2.64	5.00
Cu	21.7	56.5	54.3	13.4	39.0	340.0	659.0	47.1	6.51	63.2	253.0	93.6	38.8	31.8	24.3	25.9	66.5	0.01	5.74	46.2	5.34	26.9	5.35	24.6	628.0
Zn	70.47	56.3	74.2	45.4	63.9	50.9	68.3	69.5	55.0	66.6	28.0	37.3	37.3	57.3	12.8	36.9	49.9	26.8	48.5	19.1	46.6	49.8	22.0	41.3	37.0
Ga	30.8	45.7	41.1	14.6	24.8	35.9	50.1	27.3	24.1	31.1	13.77	32.1	45.7	29.5	18.4	37.4	25.4	22.0	34.1	35.5	28.4	32.9	39.74	37.7	14.3
As	2.41	4.15	1.11	1.61	24.8	6.10	2.04	5.50	4.25	4.23	3.23	1.19	2.05	1.86	0.87	2.10	3.19	1.53	8.05	1.42	6.49	3.01	2.78	1.35	nd
Rb	92.8	155.0	122.0	39.1	33.2	9.04	142.0	137.0	61.1	154.0	42.31	52.7	100.0	72.5	55.2	134.0	91.4	58.6	107.0	104.0	92.1	114.0	134.6	91.0	84.2
Sr	362	706	660	258	1103	871	671	391	320	322	179	767	804	383	260	525	349	313	629	586	526	390	316	149	106
Y	19.2	28.1	25.3	8.67	23.0	19.6	14.6	19.1	11.1	17.5	2.56	10.9	23.1	11.3	7.1	24.6	10.0	7.1	15.0	12.8	12.3	17.8	7.38	21.4	27.1
Zr	26.7	47.4	61.2	12.6	88.1	63.7	11.2	42.2	25.4	19.9	7.17	13.4	62.3	13.3	9.3	34.2	5.38	10.9	85.1	43.2	52.4	16.0	4.23	212.0	314.0
Nb	20.8	45.5	36.3	6.12	7.32	23.8	20.1	23.9	28.2	25.7	8.14	17.3	37.7	19.2	18.9	38.6	24.8	17.7	27.5	24.7	22.7	29.1	15.5	26.2	20.8
Cd	0.56	0.26	3.64	0.14	0.22	0.45	0.42	0.32	0.35	0.50	0.08	0.11	0.23	0.16	0.14	0.19	0.13	0.11	0.36	0.25	0.23	0.41	0.59	0.22	nd
Cs	2.49	5.04	4.01	2.08	2.39	0.32	3.65	4.96	2.39	4.64	0.52	0.26	1.37	1.16	0.30	3.26	2.27	0.43	1.76	2.32	1.52	2.28	2.01	2.86	1.21
Ba	46	768	669	238	406	666	1063	349	126	539	110	713	668	626	374	630	574	476	526	545	466	554	862	536	508
La	74.2	69.7	67.7	25.3	36.1	41.2	30.6	48.8	73.8	51.0	21.9	39.9	58.6	31	22.2	61.9	37.1	26.5	44.4	39.4	38.8	47.4	17.2	40.9	34.3
Ce	135	138	140	37.8	79.6	91.8	68.5	93.9	101.0	101.0	27.0	69.8	127	58.1	44.4	124	66.2	49.7	91.1	83.1	79.9	98.0	32.8	98.8	64.7
Pr	15.10	15.40	16.30	4.39	9.22	10.60	7.54	9.53	8.72	10.92	2.56	8.68	14.7	7.05	5.37	13.5	7.86	5.79	9.27	8.34	7.96	10.4	2.95	10.2	7.18
Nd	56.1	48.7	56.8	16.4	34.1	38.1	28.2	31.4	30.3	38.0	8.36	30.3	46.3	24.9	18.3	42.6	26.3	19.4	29.1	26.6	24.8	37.5	9.96	31.7	24.8
Sm	9.60	8.08	9.59	3.11	7.27	6.80	5.24	5.54	4.81	6.36	1.37	5.11	7.56	4.32	2.99	6.91	4.21	3.19	4.51	4.30	3.94	6.66	1.81	5.60	4.70
Eu	1.76	2.21	2.31	0.86	2.20	1.88	1.54	1.25	0.86	1.24	0.31	1.61	2.10	1.27	0.83	1.79	1.18	0.90	1.28	1.19	1.13	1.72	1.08	0.87	0.75
Gd	7.69	6.69	8.32	2.74	6.59	5.52	4.25	4.62	4.11	5.06	1.15	3.90	6.38	3.64	2.42	5.91	3.24	2.42	3.54	3.47	3.22	5.19	1.59	5.11	4.65
Tb	0.97	0.92	1.18	0.38	0.90	0.79	0.58	0.68	0.49	0.69	0.13	0.55	0.83	0.51	0.35	0.81	0.45	0.33	0.49	0.47	0.43	0.74	0.23	0.82	0.78
Dy	4.79	4.91	5.42	1.98	4.39	4.23	3.12	3.53	2.57	3.68	0.68	2.88	4.28	2.78	1.77	4.38	2.39	1.82	2.45	2.29	2.10	3.88	1.46	4.46	4.28
Ho	0.81	1.07	1.19	0.36	0.87	0.79	0.58	0.72	0.45	0.64	0.11	0.54	0.85	0.53	0.34	0.91	0.42	0.3	0.49	0.48	0.43	0.72	0.30	0.91	0.95
Er	1.97	2.73	2.69	0.86	2.23	2.04	1.45	1.83	1.14	1.77	0.28	1.29	2.18	1.35	0.81	2.36	1.09	0.83	1.27	1.24	1.17	1.83	0.75	2.50	3.06
Tm	0.26	0.41	0.39	0.12	0.31	0.29	0.20	0.27	0.15	0.26	0.03	0.18	0.31	0.2	0.12	0.35	0.15	0.12	0.19	0.16	0.16	0.27	0.11	0.36	0.44
Yb	1.52	2.55	2.20	0.81	1.93	1.77	1.19	1.57	0.98	1.55	0.21	1.16	1.92	1.25	0.82	2.22	0.97	0.75	1.18	1.11	1.07	1.62	0.69	2.22	3.22
Lu	0.24	0.38	0.37	0.12	0.27	0.28	0.19	0.25	0.16	0.24	0.04	0.16	0.27	0.19	0.11	0.31	0.13	0.11	0.16	0.15	0.15	0.27	0.11	0.32	0.55
Ta	1.64	4.63	5.86	0.59	1.00	2.90	1.41	1.93	1.26	1.95	0.35	1.3	3.64	1.09	2.78	4.19	2.35	2.34	2.64	2.54	4.36	2.74	1.68	3.67	1.60
W	0.90	5.74	0.87	1.50	2.16	15.80	2.83	6.55	1.78	5.84	0.01	1.44	1.77	0.93	0.35	2.07	3.20	0.21	0.80	10.80	0.53	7.58	16.00	1.08	3.00
Pb	9.29	20.7	76.8	3.67	9.66	15.4	5.57	20.3	9.74	17.4	3.73	14.0	11.2	14.0	8.66	12.9	20.1	9.59	12.7	10.8	10.7	14.5	21.5	20.5	17.0
Th	21.2	27.1	14.1	5.94	11	10.2	5.8	13.1	13.2	16.05	6.38	7.77	29.1	10.8	19.1	30.0	16.9	9.58	23.7	19.9	26.3	18.7	17.0	29.4	10.1
U	8.09	8.67	4.47	3.71	2.84	2.81	1.29	5.77	14.1	4.26	4.54	4.67	8.71	6.15	6.87	5.93	5.11	4.50	7.02	7.05	7.49	8.14	4.28	5.65	2.18
Hf	1.25	1.61	1.86	0.53	2.66	2.53	0.56	1.28	1.5	0.84	0.52	0.75	2.04	0.85	0.66	1.22	0.27	0.67	2.39	1.35	1.64	1.04	0.22	0.16	8.10
Sum REE	310	301	315	95.4	186	206	153	204	230	223	64.3	166	273	137	100	268	151	112	189	172	165	216	71.1	204	154
A/CNK	–	0.85	0.85	0.77	0.48	0.57	–	0.80	0.72	–	0.94	0.88	0.86	0.88	0.88	0.90	0.93	0.90	0.94	0.95	0.81	–	–	1.09	1.15
K_2O/Na_2O	–	0.82	0.85	0.65	0.66	0.12	–	0.97	0.16	–	0.37	0.82	0.94	1.09	1.61	1.38	1.3	1.31	1.17	1.11	1.04	–	–	1.37	0.76
Total alkali	–	6.96	6.37	5.76	3.51	4.48	–	7.06	5.81	–	5.91	6.86	7.18	7.54	8.85	7.81	8.08	7.99	7.66	7.61	7.60	–	–	6.37	6.56
Mg no.[b]	–	0.44	0.43	0.45	0.48	0.7	–	0.41	0.64	–	0.5	0.43	0.43	0.43	0.37	0.34	0.42	0.44	0.4	0.45	0.75	–	–	0.33	0.28
Eu/Eu*[c]	0.63	0.92	0.79	0.91	0.98	0.95	1.00	0.76	0.60	0.67	0.77	1.11	0.93	0.98	0.95	0.86	0.98	0.99	0.98	0.95	0.98	0.90	1.96	0.50	0.49
La_n/Yb_n	32.7	18.2	20.6	21.0	12.5	15.5	17.2	20.8	50.5	22.0	69.5	23.1	20.4	16.5	18.1	18.6	25.5	23.7	25.1	23.8	24.1	19.6	16.6	12.3	7.12

[a] Mdi – monzodiorite; Emz – enclave monzonite; Mz – monzonite; Pmz – pegmatitic monzonite; Gbd – gabbro-diorite; Egd – enclave granodiorite; Gd – granodiorite; Bgr – biotite granite; nd – not determined.

[b] Mg no. = mol MgO/(MgO + FeO).

[c] $Eu^* = \sqrt{Eu/(Sm^*Gd)}$.

processes involved. Major elements were analysed by X-ray fluorescence (XRF) at the University of Oviedo (Spain) using glass beads. Precision of the XRF technique was better than ± 1.5 % relative. Trace elements and rare earth elements (REE) were analysed by inductively coupled plasma mass spectrometry (ICP-MS) with a HP-4500 system at the University of Huelva, following digestion in HF + HNO_3 (8:3) solution, drying and second dissolution in 3 ml HNO_3 and later 3 ml HCl. The average precision and accuracy for most of the elements fall in the range of 5–10 %, and they were controlled by repeated analyses of the SARM-1 (granite) and SARM-4 (norite) international rock standards.

Sr and Nd isotopic compositions were determined with a Finnigan MAT 262V multi-collector mass spectrometer (at IGGI, CNR Pisa) after conventional ion exchange procedures for Sr and Nd separation from the matrix. Sr total blank was better than 2 µg while Nd total blank was less than 1 µg during the period of measurement. Measured $^{87}Sr/^{86}Sr$ ratios have been normalized to $^{86}Sr/^{88}Sr = 0.1194$; $^{143}Nd/^{144}Nd$ ratios to $^{146}Nd/^{144}Nd = 0.7219$. Results for major and trace element analyses are given in Table 1. Table 2 reports the Sr and Nd isotopic data.

Three samples containing large (> 100 µm length) zircon crystals and representing the main three intrusive groups, namely granodiorites, monzonites and monzodiorites (samples Sh-M1–9, Sh-M3–72 and Sh-M3–121, respectively) were selected for U–Pb laser ablation (LA)-ICP-MS geochronology. Zircon crystals were separated using conventional magnetic and heavy liquid techniques. Grains were handpicked and selected according to their shape and colour. They were mounted in epoxy and polished until a portion of each grain not less than 60 µm in diameter was exposed. Then, they were observed and studied for zoning and inclusions by using backscattered electron (BSE) and cathodoluminescence (CL) imaging on a JEOL JSM5410 electron scanning microscope. LA-ICP-MS analysis of Pb isotopes and ppm determinations of Ti, Zr, Hf, Th and U were carried out with a Nd-YAG 213 nm Mercantek laser and a torch-shielded quadrupole Agilent 7500 ICP-MS system at the University of Granada. A complete description of the method can be found in Bea *et al.* (2006) and Montero *et al.* (2007).

6.b. Major elements

Representative whole-rock analyses of major and trace elements from the main intrusive lithologies are shown in Table 1. Rocks of Cycle 1 (gabbro-diorites, granodiorites and biotite granites) display a wide silica range from 48 to 77 wt % SiO_2. The silica range is narrower (45–63 wt % SiO_2) for the monzodiorites and monzonites of Cycle 2. According to the Frost *et al.* (2001) classification scheme, all rocks, with the exception of the biotite granites, are metaluminous (ASI < 1). Monzodiorites and monzonites (Cycle 2) plot across the boundary between the ferroan and

Table 2. Sr–Nd isotopic analyses of representative rocks from the Shaivar Dagh intrusive complex

Rock type	Sample no.	Rb (ppm)	Sr (ppm)	$^{87}Rb/^{86}Sr$	$^{87}Sr/^{86}Sr$	$(^{87}Sr/^{86}Sr)_i^a$	±2σ	Sm (ppm)	Nd (ppm)	$^{147}Sm/^{144}Nd$	$^{143}Nd/^{144}Nd$	$(^{143}Nd/^{144}Nd)_i^a$	±2σ	$\varepsilon_{Nd}(t)^a$	T_{DM}(Ga)
Nepheline monzodiorite	Sh-M4–72	99.4	1031.4	0.2787	0.704209	0.704114	0.000009	10.31	60.54	0.1030	0.512818	0.512802	0.000010	3.80	0.53
Monzodiorite	Sh-M3–130	72.0	1113.1	0.1870	0.704648	0.704339	0.000010	10.44	57.71	0.1094	0.512766	0.512757	0.000004	3.13	0.61
Monzonite	Sh-M3–73	131.5	683.8	0.5561	0.704812	0.704344	0.000011	9.08	52.15	0.1053	0.512755	0.512739	0.000006	2.58	0.65
Diorite	Sh-M3–45	122.1	660.5	0.5348	0.704534	0.704544	0.000090	9.59	56.83	0.1020	0.512756	0.512742	0.000010	2.83	0.63
Granodiorite	Sh-M1–15	104.4	586.5	0.5150	0.704424	0.704414	0.000008	4.30	26.61	0.0979	0.512780	0.512746	0.000007	2.90	0.63
Enclave granodiorite	Sh-M4–67	137.2	391.0	1.0148	0.704787	0.704351	0.000010	5.54	31.45	0.1065	0.512763	0.512733	0.000005	2.65	0.65
Biotite granite	Sh-M3–27	91.0	149.6	1.7610	0.708804	0.708004	0.000010	5.60	31.71	0.1068	0.512449	0.512427	0.000010	−3.32	1.16

CHUR values: $^{87}Rb/^{86}Sr = 0.0847$, $^{87}Sr/^{86}Sr = 0.7047$, $^{147}Sm/^{144}Nd = 0.1967$, $^{143}Nd/^{144}Nd = 0.51263$

[a] Initial isotopic ratios for each sample are calculated at adopted crystallization age.

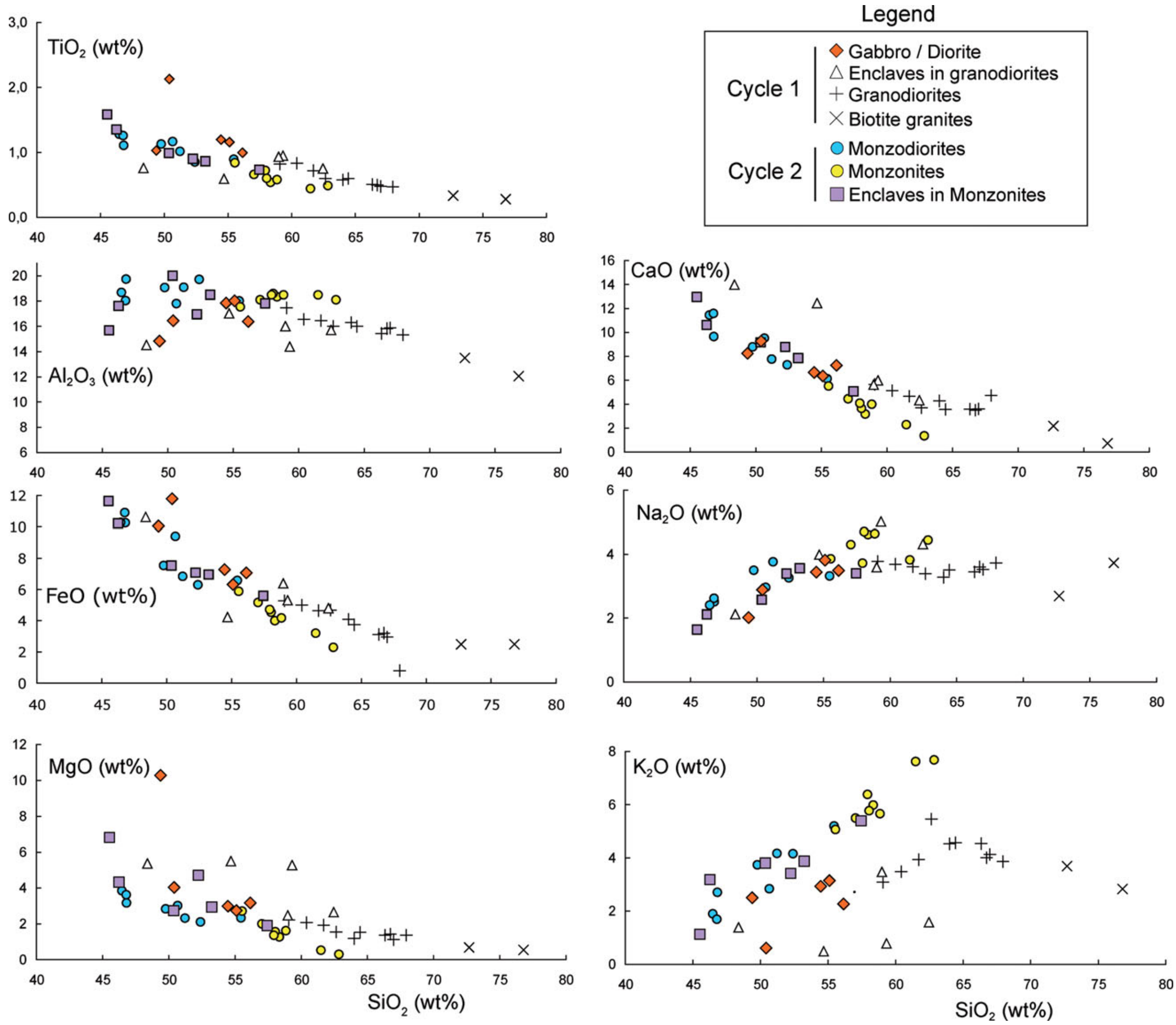

Figure 4. (Colour online) Silica variation diagrams plotting the compositions of the Shaivar Dagh intrusive complex rocks. The two magmatic cycles (calc-alkaline and shoshonitic) can be identified in these diagrams. See text for further explanations.

magnesian series, but all rocks forming the gabbro–granodiorite association (Cycle 1) are magnesian. According to the Peacock's calc-alkalic index, represented in the MALI–SiO_2 diagram (Fig. 3b), the gabbro–granodiorite rocks, and their related enclaves, plot in the calc-alkalic and alkali-calcic fields, following the trend of the field boundaries. However, rocks of the monzodiorite–monzonite association plot across the field boundaries evolving from calc-alkalic and alkali-calcic (monzodiorite) to alkalic series (monzonite). All together, the Cycle 2 rocks define a straight linear trend in the MALI–SiO_2 diagram (Fig. 3b) cross-cutting the field boundaries and almost coincident with typical potassic series of the Mediterranean province (Conticelli *et al.* 2009).

Harker variation diagrams (Fig. 4) show two well-defined linear trends for the two magmatic cycles. These are prominent in the TiO_2, MgO, CaO and K_2O diagrams. Peraluminous biotite granites are aligned with granodiorites (Cycle 1) for most major element variation diagrams. Harker diagrams are consistent with magmatic crystallization and fractionation in both cycles acting separately, corresponding to two distinct and unconnected magmatic series. There is a marked overlap between enclaves and host rocks in both series.

The two magmatic cycles are well defined in the K_2O–SiO_2 diagram (Fig. 5a). Monzodiorites and monzonites plot in the field of the shoshonitic (SH) series and most of the rocks of Cycle 1 plot in the field of the high-K calc-alkaline (HKCA) series. It is noticeable that some rocks of the HKCA series, or Cycle 1, plot in the shoshonitic area. A similar observation can be made in the diagrams K_2O/MgO v. MgO and K_2O/MgO v. SiO_2 (Fig. 5b, c). These diagrams are useful to distinguish typical calc-alkaline from monzonitic (shoshonitic) series. The lines separating these fields are empirically traced using the composition of the typical cordilleran batholiths as reference. Rocks of the HKCA series are transitional in these diagrams. Some low-silica granodiorites and quartz-diorites of Cycle 1 plot in the area of monzonites.

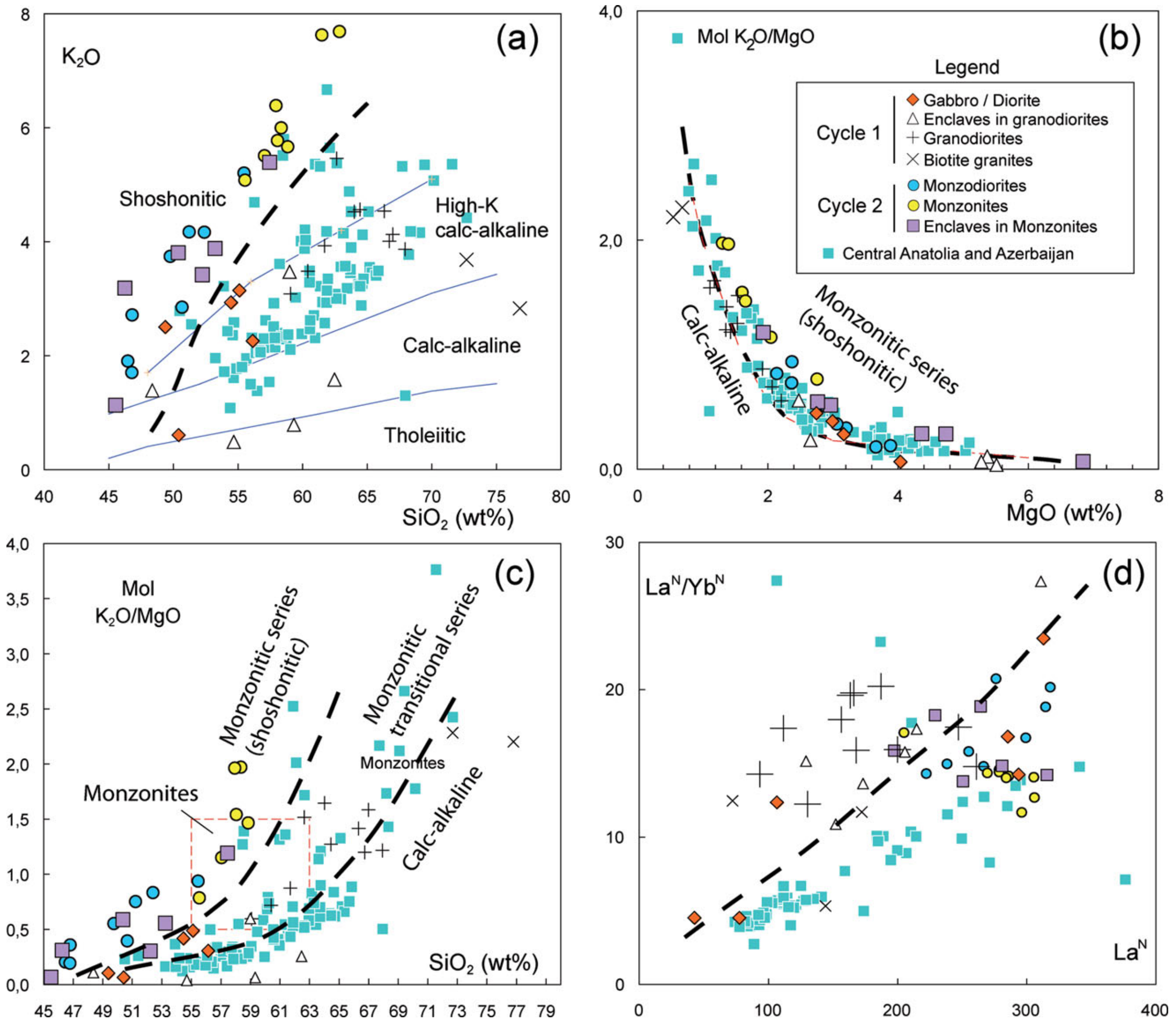

Figure 5. (Colour online) Selected diagrams showing relevant inter-elemental relationships between intrusive rocks of the Shaivar Dagh intrusive complex. In all diagrams, shoshonitic and calc-alkaline series are well distinguished. Some granodioritic rocks show transitional features that are highlighted in (a) and (c). Granodiorites form a separate group according to the La/Yb (normalized) ratios (d).

6.c. Trace elements

The distinctive characteristics of the SDIC rock cycles are clearly shown by the trace element signatures. Rocks of the SH association (Cycle 2) are characterized by low Ni contents (0.01–30 ppm) compared to the rocks of the HKCA association (Cycle 1) (2–200 ppm) (Table 1). More complex patterns are shown by Cr in both cycles, in agreement with variable clinopyroxene abundances. Variation diagrams of SiO_2 v. selected trace elements (see diagrams in online Appendix 1 at http://journals.cambridge.org/geo) display a general decrease of most compatible elements with increasing SiO_2, and increasing high field strength elements (HFSEs) (e.g. Nb) and large-ion lithophile elements (LILEs) (e.g. Rb) in both cycles. In the SH association, the Sr content decreases with increasing SiO_2, whereas it is relatively constant in the HKCA association. Ba exhibits a positive correlation with SiO_2 in the SH association and shows a complex pattern in the HKCA one. The relevant feature of the Cycle 2 samples is the high abundances of Sr and Ba. These elements vary from 368 to 2175 ppm and 364 to 1541 ppm, respectively, for Sr and Ba in the SH association (Cycle 2), and from 179 to 1104 ppm and 110 to 1063 ppm for the HKCA association (Cycle 1). Biotite granites exhibit low Sr (106–316 ppm) and high Ba (508–862 ppm) contents (Table 1).

Nearly all samples of the HKCA association display a marked negative anomaly in Hf and Zr, reaching a chondrite to slightly subchondrite level for some of them, whereas these anomalies are absent in most samples of the SH association. The SH association rocks show the typical patterns of subduction-related magmas, with enrichment in LILEs and negative anomalies in Nb and Ti. Additionally, rocks of the HKCA association show negative anomalies in Sr and P (especially in the granodiorites). All the rocks of

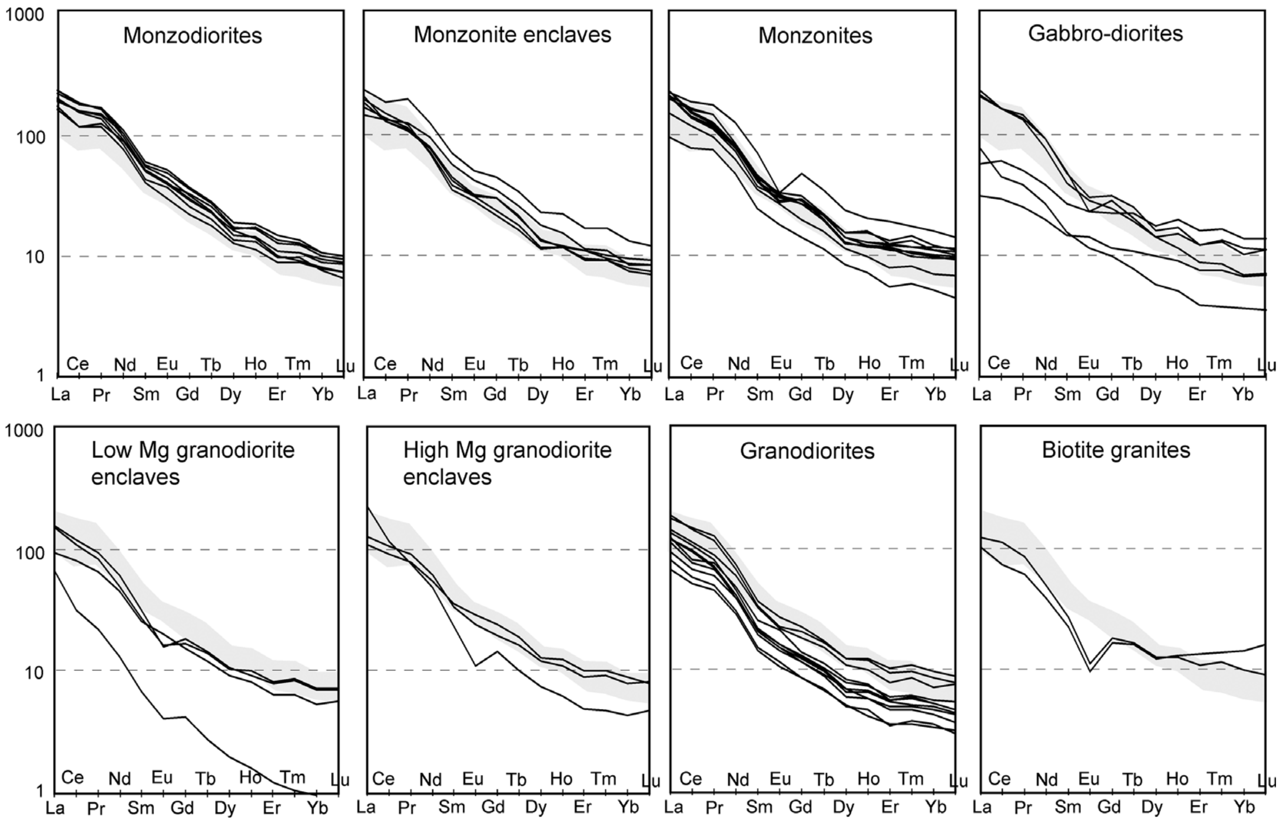

Figure 6. REE chondrite-normalized diagrams for the Shaivar Dagh intrusive complex rocks. The shaded areas in all diagrams represent the field of monzonites from the neighbouring pluton of Khankandi (Aghazadeh *et al.* 2010). All rock series (except the biotite granites) show fractionated patterns devoid of Eu anomalies.

the SDIC display strongly fractionated REE patterns in chondrite-normalized diagrams (Fig. 6) with Ce_N/Yb_N ratios ranging from 11 to 20 in the SH association, from 4 to 32 in the HKCA association and from 5 to 12 in the biotite granites. The latter show a pronounced negative Eu anomaly ($Eu/Eu^* = 0.5$) while this anomaly is almost absent in the REE patterns of the SH ($Eu/Eu^* = 0.82$–1.09) and HKCA ($Eu/Eu^* = 0.6$–1.11) associations (Table 1).

The enrichment in LILEs and light rare earth elements (LREEs), the high K_2O/Na_2O ratios and the absence of Eu anomalies are characteristic features of shoshonitic rocks (Morrison, 1980). Other salient features in all cycles of the SDIC are the negative anomalies in Nb and Ti, which are considered typical of magmas generated in subduction-related settings (e.g. Pearce, Harris & Tindle, 1984).

6.d. Sr–Nd isotopes

Seven Nd–Sr isotopic measurements (Table 2) were carried out on the SDIC. Nd–Sr isotopic data can be used to test some aspects of the petrogenetic model developed on the basis of elemental data. One nepheline-bearing monzodiorite (Sh-M4–72), one monzodiorite (Sh-M3–130), one monzonite (Sh-M3–73), one diorite (Sh-M3–45), one granodiorite (Sh-M1–15), one granodiorite enclave (Sh-M4–67) and one biotite granite (Sh-M3–27) were selected for analysis. Initial ratios are plotted in Figure 7, normalized to their absolute ages according to the results obtained from zircon radiometric dating (see Section 7). Except for the biotite granite sample, all samples show very similar Nd and Sr isotopic ratios despite their geochemical differences. Sr isotopic ratios ($^{87}Sr/^{86}Sr$ initial) vary in a limited range from 0.7041 to 0.7045. Nepheline-bearing monzodiorite and gabbro-diorites represent the lowest and highest Sr isotopic ratios, respectively. The CHUR-normalized Nd isotopic ratios vary from $\varepsilon = 2.6$ to $\varepsilon = 3.8$. The highest and lowest Nd isotopic ratios belong to nepheline-bearing monzodiorite and monzonite samples, respectively. Sr and Nd isotopic ratios of biotite granite are 0.7080 and −3.32, respectively. The depleted mantle Nd model ages (T_{DM}) of the granodiorite, diorite, monzonite, monzodiorite, nepheline-bearing monzodiorite and granodiorite enclave vary in a limited range of 0.53 to 0.65. The biotite granites represent the highest T_{DM} age (1.16).

As is shown in Figure 7, except for biotite granites, the isotopic ratios of other rock units are comparable with the neighbouring Khankandi pluton (Aghazadeh *et al.* 2010). It is apparent that except for the biotite granite, all the rock types share a common isotopic ratio, which does not necessary mean a common source as will be discussed in Section 8. Similarly to most calc-alkaline andesites, all the samples are plotted in the first quadrant of the diagram (Fig. 7). The isotopic data in the Arasbaran plutonic suites (except

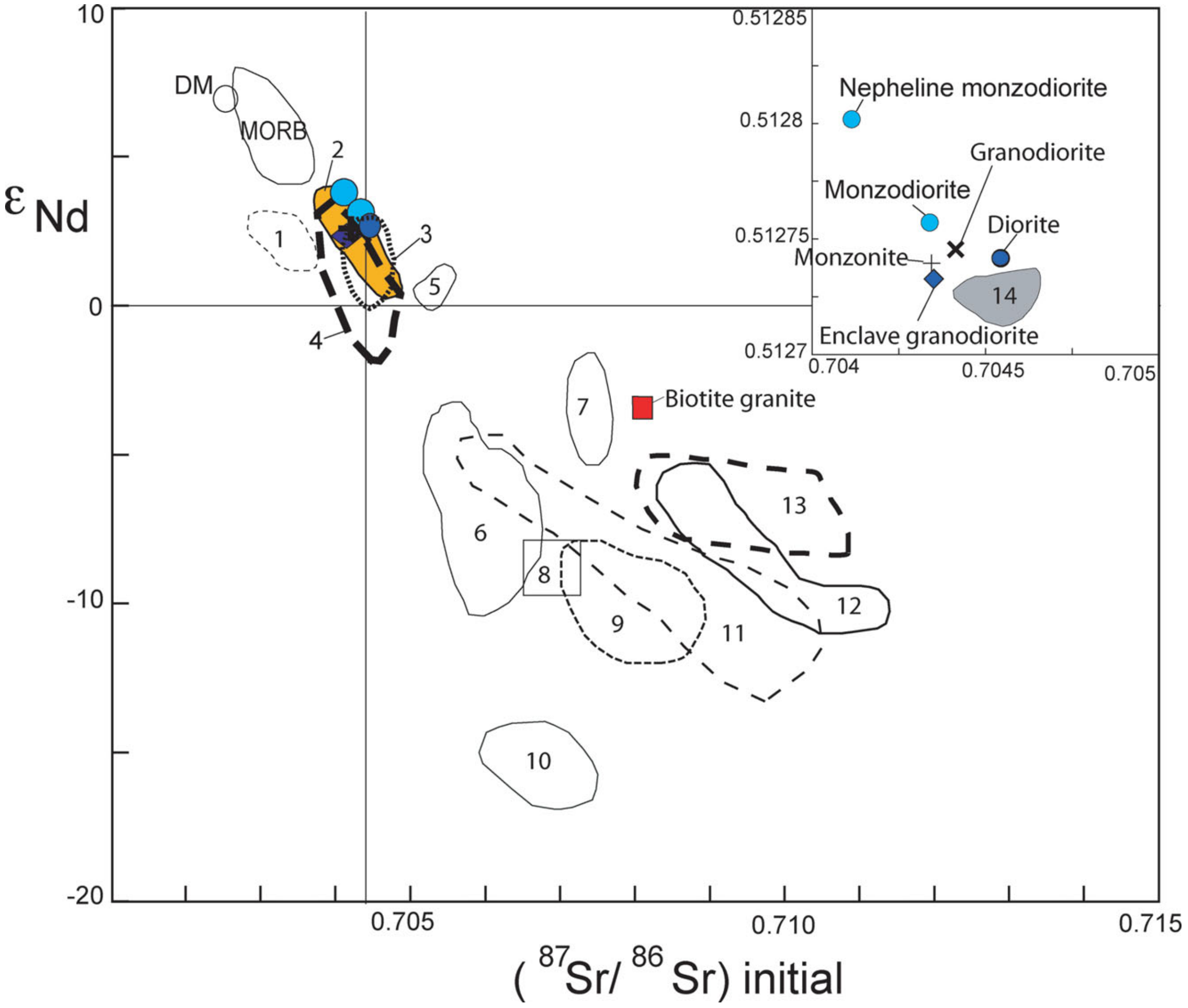

Figure 7. (Colour online) Initial Nd–Sr isotopic ratios for representative rocks of the Shaivar Dagh intrusive complex. Potassic and shoshonitic rocks and granodioritic plutons with adakitic nature from other sectors of the Tethyan orogenic belt (Tibet and Turkey) have been added for comparison. These are: 1 – Western Turkey potassic volcanics (Alici *et al.* 1998); 2 – Oligocene plutons in the southeastern part of Urumieh–Dokhtar with porphyry copper mineralization (Shafiei, Haschke & Shahabpour, 2009); 3 – Adakitic intrusives in Dexing area, south China (Wang *et al.* 2006); 4 – Glen Dessarry potassic syenitic pluton, Scottish Caledonia (Fowler, 1992); 5 – Adakitic post-collisional plutonism eastern Pontides, Turkey (Topuz *et al.* 2005); 6 – Adakitic rocks from eastern Yangtze Block, south China (Xu *et al.* 2002; Wang *et al.* 2004*a,b*); 7 – Northern Tibet K-rich adakitic volcanic rocks (Wang *et al.* 2005*b*); 8 – Adakitic intrusives from east China (Xu *et al.* 2002); 9 – Ultrapotassic volcanic rocks from central Anatolia, Turkey (Alpaslan *et al.* 2006); 10 – Sulu belt post-orogenic syenites, south China (Yang *et al.* 2005); 11 – Central Italy potassic and ultrapotassic rocks (Conticelli & Peccerillo, 1992); 12 – alkaline syenites from eastern Cathaysia, south China (Wang *et al.* 2005*a*); 13 – Northern Tibet potassic volcanic rocks (Turner *et al.* 1996); 14 – Khankandi pluton isotopic field (Aghazadeh *et al.* 2010); Mantle end-members (Zindler & Hart, 1986). MORB – mid-ocean ridge basalt; DM – depleted mantle.

for biotite granites) imply that a mantle component was largely involved in the origin of the rocks, whereas crustal processes (e.g. melting, crustal contamination and assimilation) are rare or not important. The fact that the HKCA (gabbro-diorite and granodiorite) and SH (monzodiorite and monzonite) associations share a common isotopic signature, poses an interesting problem that can be solved if all magma series were produced from a common source.

7. U–Pb zircon geochronology

Zircon crystals from granodiorite, monzonite and monzodiorite were selected for age determination using a LA-ICP-MS technique. This technique has been shown to be useful for dating only old zircon grains with abundant radiogenic Pb. In the case of the Tertiary grains analysed here, the application of this technique requires the use of a defocused beam to produce a large amount of the extracted sample. Fortunately, this is possible in rock types of the SDIC that contain large zircon crystals (>200 μm). The granodiorites contain smaller zircon crystals than the monzonites and monzodiorites.

The studied zircons in the monzonite and monzodiorite rocks have a euhedral to subhedral shape (prismatic) and pale pink colour. Zircons of the granodiorite are white to colourless and are longer and thinner

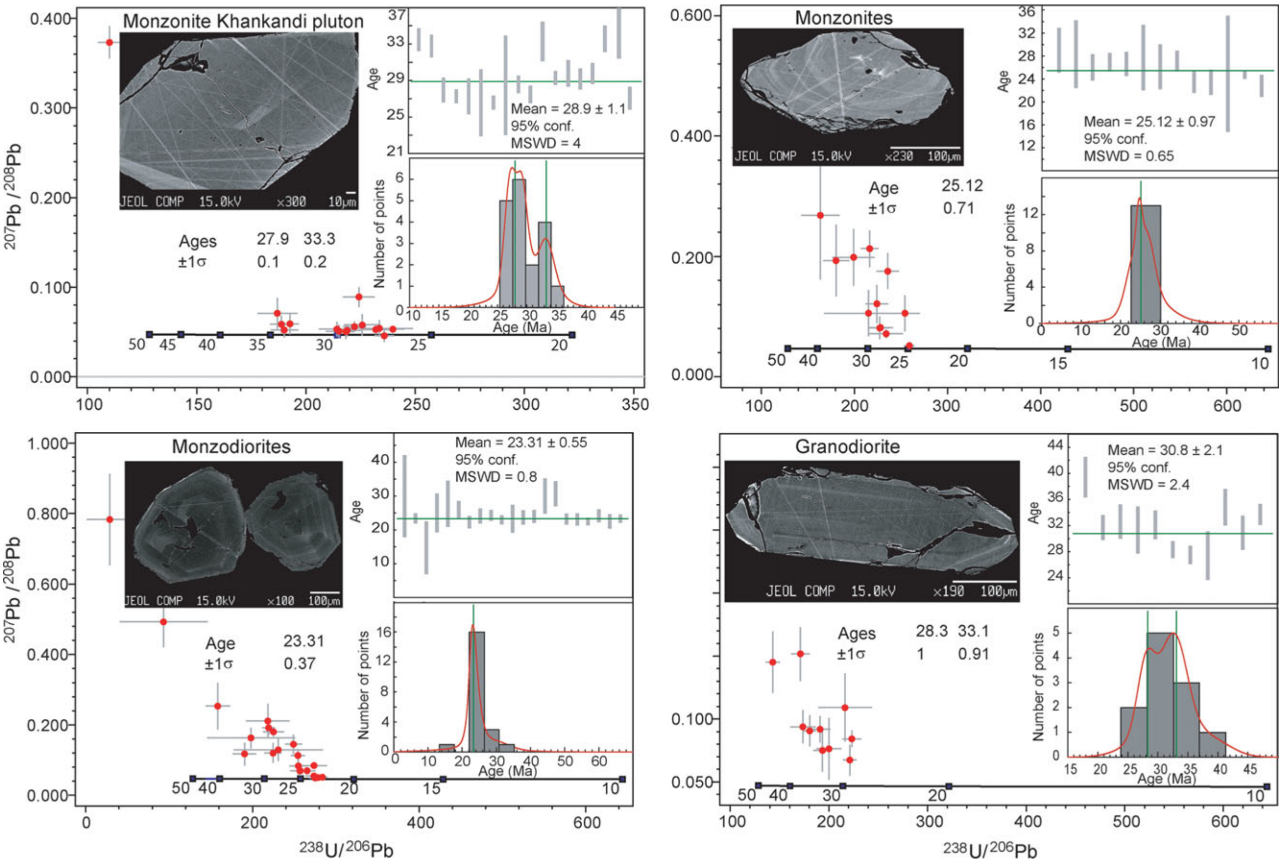

Figure 8. (Colour online) Tera-Wasserburg diagrams showing U–Pb, LA-ICP-MS of zircons from representative plutonic rocks of the Shaivar Dagh intrusive complex: monzonite (sample Sh-M3-72), monzodiorite (sample Sh-M3-121) and granodiorite (sample Sh-M3-15). A monzonite from the neighbouring Khankandi pluton (Aghazadeh *et al.* 2010) is included for comparison. MSWD – mean square weighted deviation.

than those of the monzonites and monzodiorites. In all the studied rocks, zircon crystals show well-developed oscillatory zoning indicative of magmatic crystallization without any inherited cores. The number of point analyses were 21, 13 and 11 from the different crystals of the monzodiorite, monzonite and granodiorite, respectively. The results are shown in Tables A1, A2 and A3 in online Appendix 2 at http://journals.cambridge.org/geo. The monzodiorite zircons contain a wide range of U (214–1610 ppm) and Th (148–3241 ppm) concentrations. U and Th values in the monzonite zircons vary from 303 to 662 ppm and 171 to 1026 ppm, respectively. Measured values in the granodiorite zircons are within the range 129–905 ppm U and 137–1221 ppm Th (Tables A4, A5 and A6 in online Appendix 2 at http://journals.cambridge.org/geo). The measured Th/U ratios for the monzodiorite, monzonite and granodiorite are 0.2–2.73, 0.53–1.54 and 0.63–1.34, respectively. These values are within the range commonly observed in zircon crystals from metaluminous igneous rocks. The Th/U ratio in the monzonite (0.9) is lower than monzodiorite (>1) and granodiorite (>1).

An average age of 24.3 Ma (Table A1; Fig. 8) is obtained for the monzodiorites. The maximum and minimum ages in the monzodiorites are 30.7 Ma and 14.7 Ma, respectively. The concordia age for these monzodiorites at the 95 % confidence level is 23.31 ± 0.37 Ma (Fig. 8). In the age histogram, most data are clustered between 23 and 25 Ma. The average age for the monzonite is about 25.9 Ma (Table A2). The maximum and minimum ages measured in the monzonites are 29 Ma and 22.8 Ma, respectively. Most monzonite age determinations are clustered within the interval 24–27 Ma. The concordia age for monzonites at the 95 % confidence level is 25.12 ± 0.71 Ma (Fig. 8). According to age determinations and field observations, it is concluded that the monzonites and monzodiorites intruded as alternate pulses. The average age of the granodiorites is 31.8 Ma (Table A3). The maximum and minimum ages in these rocks are 39.4 Ma and 27.4 Ma, respectively. In the age histogram, most of the results are scattered between 31 and 33 Ma.

8. Discussion

8.a. Ages and pressure–temperature conditions of crystallization

According to the field observations and distribution of the ages in the histograms, the monzonites and monzodiorites intruded as discrete magma pulses separated in time by about 2 Ma. The fact that the

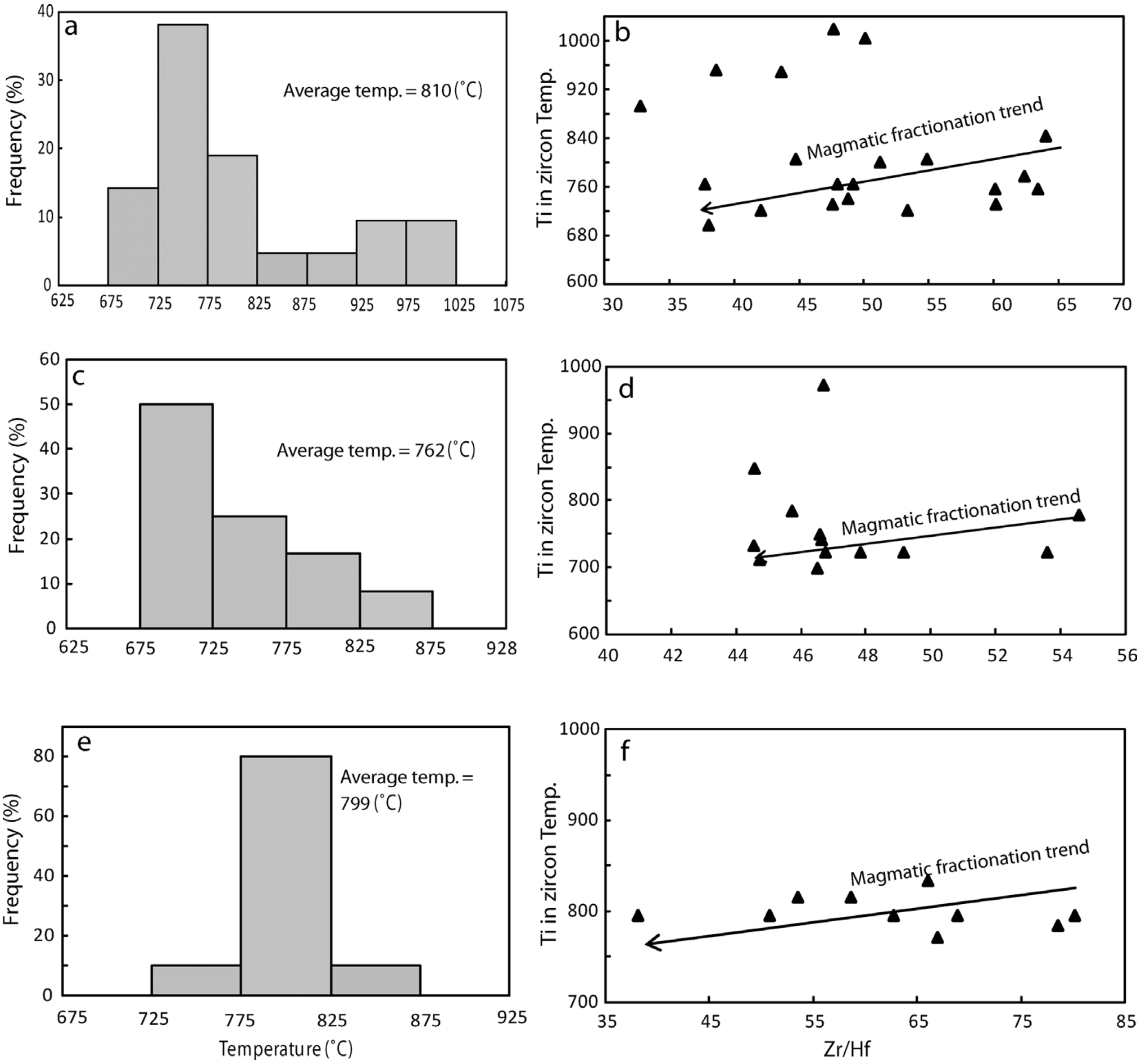

Figure 9. Frequency of temperature measurements in zircon grains and Ti-in-zircon temperatures v. Zr/Hf ratio in zircons from monzodiorite (a, b), monzonite (c, d) and granodiorites (e, f).

older is the more evolved (monzonite) and the younger the more primitive (monzodiorite) makes derivation of one series from the other by a process of magmatic fractionation unlikely. Field relations as well as age dating showed that granodiorites and related gabbro-diorites are the oldest intrusives in the SDIC.

According to these preliminary age determinations and the previously published data from the same region (Aghazadeh *et al.* 2010), and in combination with field observations, we state that plutonism in the Arasbaran zone within the Zagros hinterland started with the emplacement of gabbro-diorites and granodiorites (Cycle 1) and was followed by monzodiorites and monzonites (Cycle 2). The emplacement of lamprophyric dykes is the final manifestation of the Oligocene–Early Miocene magmatism in the zone (M. Aghazadeh, unpub. Ph.D. thesis, Tarbiat Modares Univ., 2009; Aghazadeh *et al.* 2010).

The Ti-in-zircon thermometer (Watson & Harrison, 2005) is applied here to constrain the crystallization history of the magmatic rocks. Although the thermometer was originally calibrated for systems with TiO_2 activity of unity, it has been argued that rocks with similar Ti-bearing mineral assemblages would give comparable results, and that the differences in temperature recorded by zircon grains from the same rock would accurately reflect its thermal history (Watson & Harrison, 2005). Average temperatures of 810 °C, 762 °C and 799 °C are obtained for zircon crystallization in the monzodiorite, monzonite and granodiorite, respectively (Tables A4, A5 and A6; Fig. 9). The positive correlation between the Zr/Hf ratio and Ti-in-zircon temperatures (Fig. 9) confirms that zircon crystals are magmatic (Bea *et al.* 2006; Watson & Harrison, 2005). The measured Zr/Hf ratios in the zircon crystals (monzodiorite: 33–64, monzonite:

44–54 and granodiorite: 38–80) are higher than the ratios in the respective whole rocks (48, 32 and 32, respectively). This indicates that the system was depleted in Hf relative to Zr before zircon crystallization and that once saturation was reached, zircon grew continuously from a progressively cooler and increasingly Zr-depleted environment (Bea *et al.* 2007).

Pressure estimations are based on the Al content of calcic amphiboles in the porphyritic granodiorite. These granitoids have the appropriate buffering assemblage of hornblende + biotite + plagioclase + quartz + sanidine + magnetite (Johnson & Rutherford, 1989) and are thus suitable for estimation of crystallization pressure. A pressure of about 0.4 to 2 kbar (calibration by Schmidt, 1992) is obtained. This is in agreement with the thickness of the Eocene and Cretaceous deposits (<6 km) that overlay the host of the SDIC.

8.b. Magma sources

It is clear from the observation of the Harker diagrams and other inter-elemental variations that fractionation played an important role in producing, at least in part, the observed compositional trends in the SD intrusive rocks. However, no fractionation process can relate the two magmatic cycles to each other. The available data point to two genetically separated magmatic episodes. Thus, this discussion will be about the problem of the generation of two separate magmatic processes with a small difference in age of only a few million years that coalesced within a common place in the uppermost part of the crust. The origin of the parental magmas that gave rise to the two magmatic cycles is considered in the first instance. This discussion may contribute to a better understanding of lithospheric processes during extensional post-tectonic or late-tectonic regimes.

8.b.1. Origin of the gabbro-diorite–granodiorite association (Cycle 1)

Magmatic rocks of Cycle 1 show all the features that characterize calc-alkaline intrusions in post-collisional environments and continental magmatic arcs (e.g. cordilleran batholiths). Almost identical associations, with dominant granodiorites and tonalites and subordinate gabbros and diorites, are found in the late, post-collisional calc-alkaline batholiths of the European Variscides or the Newer Caledonian batholiths of northern Scotland (Stephens & Halliday, 1984; Holden, Halliday & Stephens, 1987; Fowler *et al.* 2008), which have been classically related to 'post-collisional uplift' (Pitcher, 1997). Few differences are found between these so-called 'I-Cordilleran' batholiths compared with the 'I-Caledonian' referred to as post-collisional. They are apparently unrelated to tectonic processes and, by consequence, apparently unrelated to subduction, as it has been pointed out in several recent studies that applied terms like 'within-plate' magmatism (Scarrow *et al.* 2009) or 'continental adakites' (Xiao & Clemens, 2007) to refer to these post-collisional batholiths. Consequently, the problem is of very general outreach. Paradoxically, these post-collisional calc-alkaline intrusions have all the geochemical signatures of continental arc magmas similar to the large batholiths of active continental margins. They may even have in many cases adakitic signatures like those of the Qinling orogen in the suture of the North China craton (Xiao & Clemens, 2007) and the large adakitic post-tectonic intrusions of the Ghandese batholith in South Tibet (Gao *et al.* 2010). Collision-induced slab break-off has been suggested to account for the generation of syn- and post-collisional melts from collision zones (Haschke & Ben-Avraham, 2005).

Subduction and post-collision magmatism are not, however, incompatible processes as proposed recently by the joint application of numerical thermomechanical models of the suprasubduction mantle wedge and experimental results from melting of subducted mélanges (Castro *et al.* 2010). Numerical modelling of the suprasubduction mantle wedge (e.g. Gerya, Yuen & Sevre, 2004) predicts a long-lived formation of fertile silicic plumes that may reside for several tens of million years beneath the lithosphere until the optimal conditions for ascent and emplacement into the continental hanging wall are established. These conditions are encountered when lithosphere is extended owing either to roll-back of the subducting plate or fluid-assisted weakening of the hanging wall lithosphere (Sizova *et al.* 2010). Consequently, far from being incompatible, post-collisional magmatism may be the consequence of the subduction process that preceded continental collision. According to mélange subduction models (Castro *et al.* 2010), fertile source rocks represented by subducted mélanges are cooked in the form of mantle wedge plumes several tens of millions of years before the emplacement of magmas into the continental hanging wall. Moreover, granodiorite magmas coming from melting of the composite mélanges are accompanied by potassic (shoshonitic) magmas (Cycle 2) that may have been originated by partial melting of the metasomatized mantle aureole surrounding silicic plumes. Consequently, a petrogenetic study of these two magmatic cycles is of special interest to understand processes in post-collisional environments.

According to the petrological and geochemical data from the SDIC, the rocks of Cycle 1 belong to two distinct magmatic series from distinct sources. The gabbro-diorite series comes from the peridotite mantle, which is being hydrated and melted by the action of fluids coming from the intruding and dehydrating plumes. The granodiorite series comes from melting of a silicic hybrid mélange, which is composed of oceanic crust and sediments. This mélange is molten partially at high melting rates, at conditions of the sub-lithospheric mantle, and produces silicic magmas of andesite to tonalite and granodiorite compositions. These two series, which are common in any calc-alkaline batholith, come from two distinct sources, namely mélange and hydrated mantle, but they share a common crustal, isotopically evolved contaminant represented by subducted sediments. These form part of the subducted mélange and, at the same time, contaminate the mantle wedge by fluids or melts derived from the molten mélanges. In the hypothetical case of sediment-poor plumes, the melts can be of adakitic (dacitic) composition. The so-called 'adakitic signature' defined by a high Sr/Y ratio (>20) and a strong fractionation of REEs ($(La/Yb)_N > 20$) is only an indication of the pressure of magma generation and segregation (Moyen, 2010) and has no meaning for the composition of the source. Experiments carried out at conditions of the silicic plume emplacement below the lithosphere (1.0 to 1.5 GPa and 1000 to 1100 °C; Castro *et al*. 2010), the garnet stability curve cross-cuts the P–T region of plume emplacement. Thus, the generation of magmas, either granodioritic or tonalitic, containing an adakitic signature (Grt in the source) is only dependent on the particular zone of a single plume at which the magmas are segregated. Consequently, the petrogenesis of the magmatic series of Cycle 1 in the SDIC is compatible with such a model based on the formation of silicic plumes in the suprasubduction mantle wedge (Castro *et al*. 2010). A prediction from this model, which is supported by laboratory experiments (Castro & Gerya, 2008), is that plumes may survive within the mantle until conditions of lithosphere extension, possibly related to slab roll-back, provoke the ascent of the plume and the intrusion of the magmas into the extending continental crust. The application of one of these thermomechanical models is explained in Section 8.c in detail. Here in the next Section we address separately the origin of the monzodiorite–monzonite magmatic series of Cycle 2 of the SDIC.

8.b.2. Origin of the monzodiorite–monzonite association (Cycle 2)

The wide compositional range displayed by fine-grained magmatic enclaves included into the monzonites can be taken as an indication of repeated liquid input to the magma chamber. This is based on the interpretation that enclaves represent unfractionated magma batches from the source region that quenched against the colder host at the first stages of magma emplacement. Alternatively, they may represent fractionated liquids that evolved in a deeper magma chamber before final emplacement in the shallow pluton reservoir. Geochemical relationships strongly support that rocks of this cycle are related by fractionation. However, some detailed features of the magmatic trends point to more complex relations than simple magmatic fractionation from a common parental magma. The above observations about the varied compositional spectrum of enclaves support this general observation about complex processes. Looking carefully at the variation diagrams (Fig. 4) it can be appreciated that monzodiorites and monzonites form two distinct magmatic series. For instance, they follow almost parallel trends that do not encounter each other in the MgO–silica and FeO–silica diagrams, among others. In order to make clear that we are dealing with a multi-pulse evolution involving distinct parental magmas with differences in composition, we have modelled liquid lines of descent using the MELTS code (Ghiorso & Sack, 1995) at different pressures (300 and 800 MPa) and using two starting compositions corresponding to the less evolved terms, or 'heads', of the trends observed in the diagrams. The results of this comparative study are shown in the plots of Figure 10. Low-pressure (300 MPa) fractionation curves are closer to the trends defined by rock compositions compared with high-pressure model liquid compositions, which depart considerably from the rock patterns (Fig. 10a, c). In the CaO–MgO diagram (Fig. 10b), geochemical trends and models represent cotectic evolutions dominated by the joint crystallization of plagioclase and pyroxene. Although low-pressure cotectic liquids tend to dissolve more Mg compared to high-pressure liquids, the differences between the two trends are higher than predicted by models for a pressure change from 800 to 300 MPa (Fig. 10b). Low-pressure fractionation of two distinct liquids is the most plausible interpretation. Most enclaves correspond to the low-silica monzodiorite series (LSM), but some are closer to the high-silica monzonite series (HSM), supporting that at least two parental magmas were involved in the generation of the two series. The variation in the K_2O/MgO ratio is of interest because phlogopite plays an important role in K-rich systems accounting for the observed variations. The variation of this ratio with fractionation (e.g. with SiO_2; Fig. 10c) is steeper at high-pressure compared with low-pressure evolution. The coexisting mineral assemblage determines these slopes and, in this case, it can be appreciated that low-pressure fractionation is preferred to account for the typical monzonitic composition of the HSM series and also to account for the trend displayed by the LSM series. A jump between the two series, HSM and LSM, similar to that displayed in Figure 10b, is shown by plotting the K no. (K no. = molar $K_2O/(K_2O + CaO)$) against the MgO content (Fig. 10d). Again, fractionation from a single parental magma cannot account for this compositional jump in the K no. ratio. This ratio is strongly controlled by the crystallization of pyroxene and/or plagioclase. It increases with fractionation and decreases at high degrees of crystallization owing to the precipitation of phlogopite in the system. However, no jump of the K no. ratio is expected to occur in the system. Low-pressure fractionation from two distinct parental liquids is likely for this particular case.

The differences in composition between the two fractionating liquids are reduced. The LS model is taken from enclave Sh-M3–82 and the HS one is taken from the enclave Sh-M3–117 (Table 1). These differ mainly in the silica and MgO contents. The HS model liquid is considerably more fractionated in the

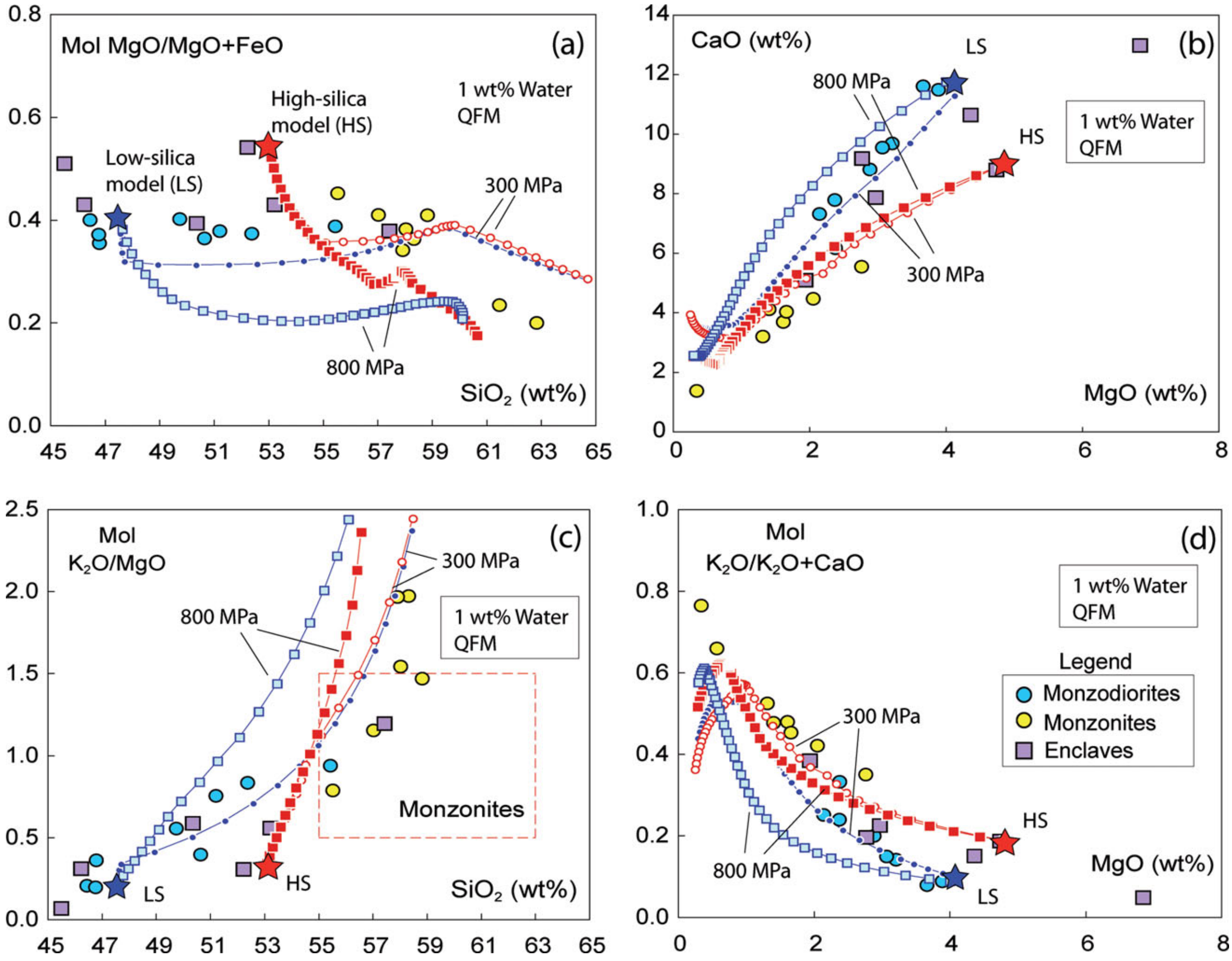

Figure 10. (Colour online) Selected geochemical diagrams showing the comparison between the two main series represented by monzonites (high-silica series) and monzodiorites (low-silica series) identified in the Shaivar Dagh pluton and model liquid lines of descent calculated with MELTS code (Ghiorso & Sack, 1995). The initial compositions, or parental liquids, used in the MELTS calculations correspond to two fine-grained enclaves that are assumed to represent quenched liquids of early injections or chilled margins of early magma pulses. Model liquid lines of descent were calculated at 300 and 800 MPa for an initial water content of 1 wt % and oxygen fugacity set at the QFM buffer (further explanations in the text).

sense that it is poorer in MgO and richer in silica. However, derivation of the HS from the LS melt is very unlikely. Most probably they represent primary liquids formed by different degrees of melting from the same source or, alternatively, from sources with slight local differences in composition. The fact that the two series are systematically present in other plutons in the area (e.g. Kankhandi; Aghazadeh *et al.* 2010) and the regular rock association in only two well-defined groups in the SDIC, point to variations in the process of melting as related to the thermal-compositional structure during decompression, rather than to local compositional heterogeneities of the metasomatized mantle source. Decompression melting is proposed on the basis of comparison with experimental results as discussed next.

According to the detailed experimental work by Niida & Green (1999), the subsaturated solidus of the metasomatized mantle is controlled by complex dehydration reactions involving pargasitic amphibole. The composition of pargasite in a metasomatized mantle system is strongly dependent on pressure, temperature and bulk peridotite composition. The subsaturated solidus may be shifted to higher temperatures for alkali-rich peridotites. However, with independence of bulk composition, the Clapeyron slope of the solidus is positive for pressures lower than 2.5 GPa. The implication is that decompression of the metasomatized mantle source may produce melting at variable degrees depending on the initial *P*–*T* location of particular zones before decompression. The pargasite breakdown reactions are continuous over a limited *P*–*T* range. Thus the amount of pargasite in the source region determines the fertility of the metasomatized mantle. Strongly metasomatized regions will be richer in pargasite, and consequently more fertile, compared with less metasomatized zones. Although melting reaction may be complex, owing to the complex solid solutions of amphibole (Niida & Green, 1999), the composition of melts formed by pargasite breakdown may be homogeneous within a given pressure region (i.e. Pl, Spl or Grt) and not dependent on the amount of pargasite present in a particular area of the metasomatized mantle. Near-solidus melts are silica-rich shoshonites according to experiments reported by Conceição & Green (2004). However, within the supersolidus region far from the solidus and the stability field of pargasite, the composition of melts will change by intervening other mafic minerals (Px and Ol) and, thus, increasing the ferromagnesian components and decreasing the silica content. Melting at supersolidus conditions of a pargasite peridotite is under study at present. Our preliminary results (A. Castro *et al*. unpub. data, 2011) indicate that these melts may range from shoshonitic to low-silica monzodiorites and lamproites by increasing temperature up to 1200 °C, that is 150 °C higher than the solidus at 1 GPa. Application of these general experimental constraints to our study implies that the two potassic series can be derived by variable melting rate of a pargasite peridotite source. Low melt fractions can be formed just close to the solidus and high melt fractions at the supersolidus region. Decompression alone may help to reach supersolidus conditions of an ascending metasomatized mantle. However, according to the pargasite-breakdown melting curves shown in Figure 11, an additional heating is necessary to get supersolidus conditions required for lamproitic melt compositions. New thermomechanical models are needed to get a more accurate image of the thermal structure of a decompressing mantle. Hypothetical inferences can be addressed here by taking into account the present-day knowledge about the thermal structure of the mantle in subduction zones. These inferences are only tentative approaches, but their analyses may help to understand the complex processes involved in post-collisional magmatism in areas that underwent previous episodes of subduction at an active continental margin. These are summarized here in the next Section.

8.c. Application of thermomechanical models to magma generation in the Zagros hinterland

It is inferred from the chemistry of the magmas and the constraints imposed by laboratory experiment on phase equilibria and melt compositions (Niida & Green, 1999; Conceição & Green, 2004) that partial melting of a metasomatized mantle is the most plausible interpretation for the origin of the shoshonitic series that produced the post-collisional monzodiorites and monzonites of the SDIC. However, the question of how this metasomatized mantle is generated remains controversial. The classical view is that mantle metasomatism is produced by fluids released from dehydration reaction of the subducting slab. However, the location of the metasomatized mantle source just beneath the magmatic arc is far away from the zone of peridotite–fluid interaction in the vicinities of the subduction channel. It is not expected that fluids can travel large distances in the peridotite mantle. Fluids, melts or supercritical fluid phases will be consumed in hydration reactions with the peridotite mantle giving rise to serpentinites at $T <$ 500 °C and to hydrous mantle assemblages dominated by amphibole and phlogopite at higher temperatures. If local temperatures overpass the hydrated solidus of the peridotite, fluids will be dissolved in melts impeding further transportation. In summary, the circulation of fluids through the mantle is very unlikely (Thompson, 1992). Counter flow of the whole mantle wedge is hypothetically proposed (Tatsumi, 1989) to account for transportation of the metasomatized areas of the mantle to hot regions below the magmatic arc. However, the distribution of hydrated mantle zones is dependent on the stability of hydrous minerals and particularly the stability of pargasite, which dominates the hydration reactions in the hot mantle (Niida & Green, 1999). Consequently, the key question to understand the generation of magmas from a metasomatized mantle source is to decipher which is the mechanism that produced metasomatized zones in the mantle in places favourable for melting and magma generation.

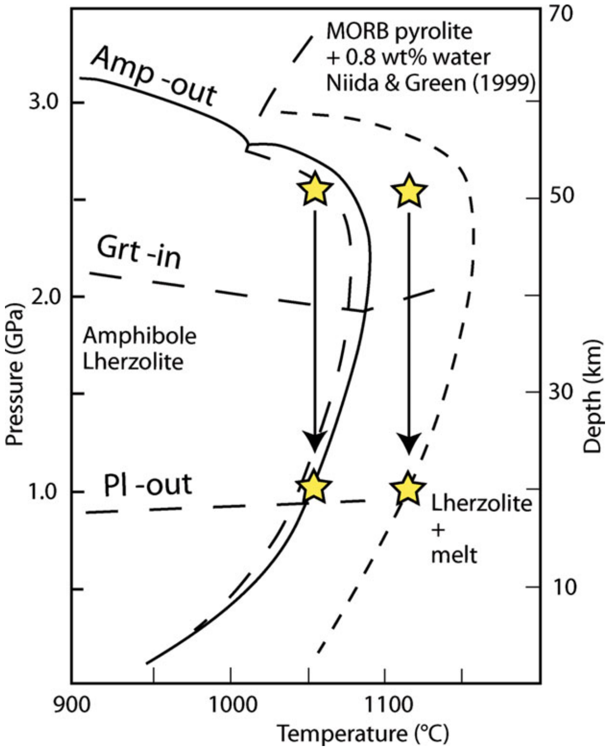

Figure 11. (Colour online) Pressure–temperature diagram showing the location of the subsaturated solidus of pargasite lherzolite. The low *T* curve (solid line) is from Niida & Green (1999) and the high *T* curve (short dashes) is from Green (1973). The differences between these two amphibole breakdown curves are due to the effect of the bulk composition of the peridotite. Arrows mark possible decompression trajectories of two points in the metasomatized aureole around a silicic plume in the mantle wedge. These may account for the observed differences in composition between the two potassic series of the Shaivar Dagh intrusive complex. The high-silica (HS) series can be formed close to the solidus and, thus, represent low melt fraction melts. The low-silica (LS) series can be formed by high melting rates at pressures far below the subsaturated solidus.

Numerical thermomechanical modelling of subduction zones below active continental margins have been addressed in order to determine the thermal

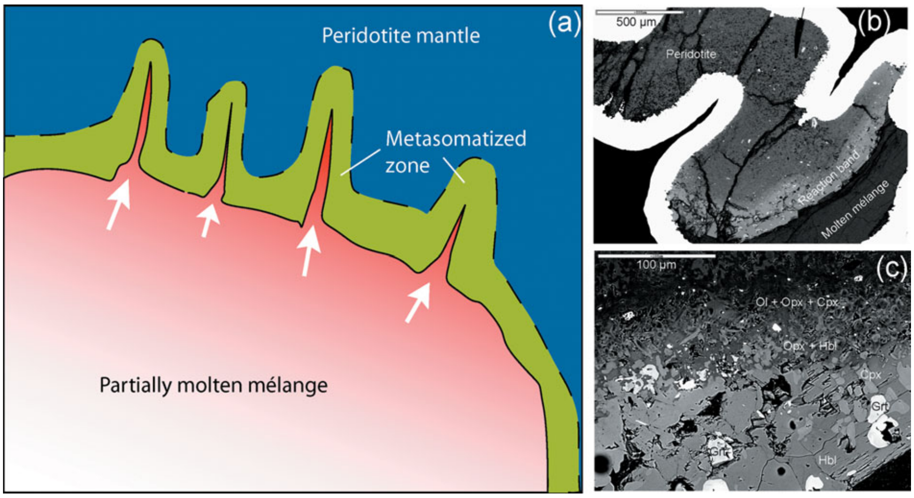

Figure 12. (Colour online) (a) Schematic diagram showing the location of the metasomatized aureole around a silicic plume. The metasomatizing agents can be melts or fluids expelled out from the silicic magma chamber. (b) and (c) Formation of hornblende (pargasite)-rich bands by reaction between mélange and peridotite based on previous experimental work (Castro & Gerya, 2008).

structure and time evolution of the mantle wedge. The results will be used to locate potential magma sources and melting reactions according to phase equilibria experiments. The close association between granodiorite magmas, derived from silicic plumes rooted in the subduction channel, and shoshonitic magmas derived from metasomatized regions of the mantle, as is found in the SDIC, is of great interest. The process of metasomatism and melting within the mantle wedge closely relates both magmatic series: fluids and/or melts of the silicic plumes emplaced into the mantle wedge just beneath the lithosphere can be injected along veins into the surrounding mantle (Fig. 12), producing a metasomatized aureole rich in pargasitic amphibole. This inference is based on previous studies about silicic magma generation from mantle wedge plumes (Castro & Gerya, 2008; Castro *et al.* 2010). The result of thermomechanical simulations of subduction at active continental margins is used here as the starting point of a hypothetical evolution from subduction to continental collision and post-collisional lithosphere extension. The post-subduction evolution, shown in a cartoon in Figure 13, is highly hypothetical. However, in comparison with other models, in this case the starting point is a thermal structure resulting from a numerical simulation carried out in the following way.

The model followed here is similar to the one explored by Sizova *et al.* (2010) and simulates the processes of forced subduction of an oceanic plate beneath a continental plate, including spontaneous slab retreat and bending, dehydration of subducted crust, aqueous fluid transport, partial melting, melt extraction and melt emplacement in the form of extrusive volcanic rocks and intrusive plutons. Previous experiments have shown that the transition between different geodynamic regimes is closely linked to the weakening effects of fluids percolating from the subducting slab into the mantle wedge and upward propagating melts (Sizova *et al.* 2010). Reduced fluid-related weakening leads to strong coupling of the plates, enhances sediment subduction, triggers sediment erosion and facilitates underplating plumes. In the course of subduction, water is expelled owing to compaction or as a result of metamorphic dehydration reactions. Aqueous fluids percolating from the slab into the mantle wedge may either form a serpentinized layer above the slab (depth < 130 km) or induce partial melting (depth > 100 km). In addition, basalts and sediments along the slab are localized. All these processes induce Rayleigh–Taylor instabilities along the slab and generate cold plume upwellings (Gerya & Yuen, 2003). The hybrid source of these upwellings, which are composed of partially molten sediments and basalts with some contribution of hydrated mantle, results in the formation of silicic plumes. Subsequently, the plume detaches from the slab and underplates the continental lithosphere, remaining there for up to 20 Ma.

8.d. Compatibility between subduction and post-collisional magmatism

The overall enrichments in LILEs and LREEs with negative Nb–Ta–Ti anomalies are features of subduction-related magmas and are commonly attributed to a mantle source that has been previously enriched in LILEs over HFSEs by metasomatic activity of fluids derived from the subducted slab or sediments (e.g. Pearce, 1983; Hawkesworth *et al.* 1997; Elburg *et al.* 2002). In the Arasbaran area, however, an active subduction system during Oligocene–Miocene times is not reported. Nevertheless, the high LILE/HFSE ratios and negative Nb, Ta and Ti anomalies can be also characteristics of magmas originated from an enriched subcontinental lithospheric mantle caused by earlier subduction episodes. The depletion in Nb, Ta and Ti can be explained also by retention in Ti-rich residual mineral phases (i.e. rutile, titanite) in

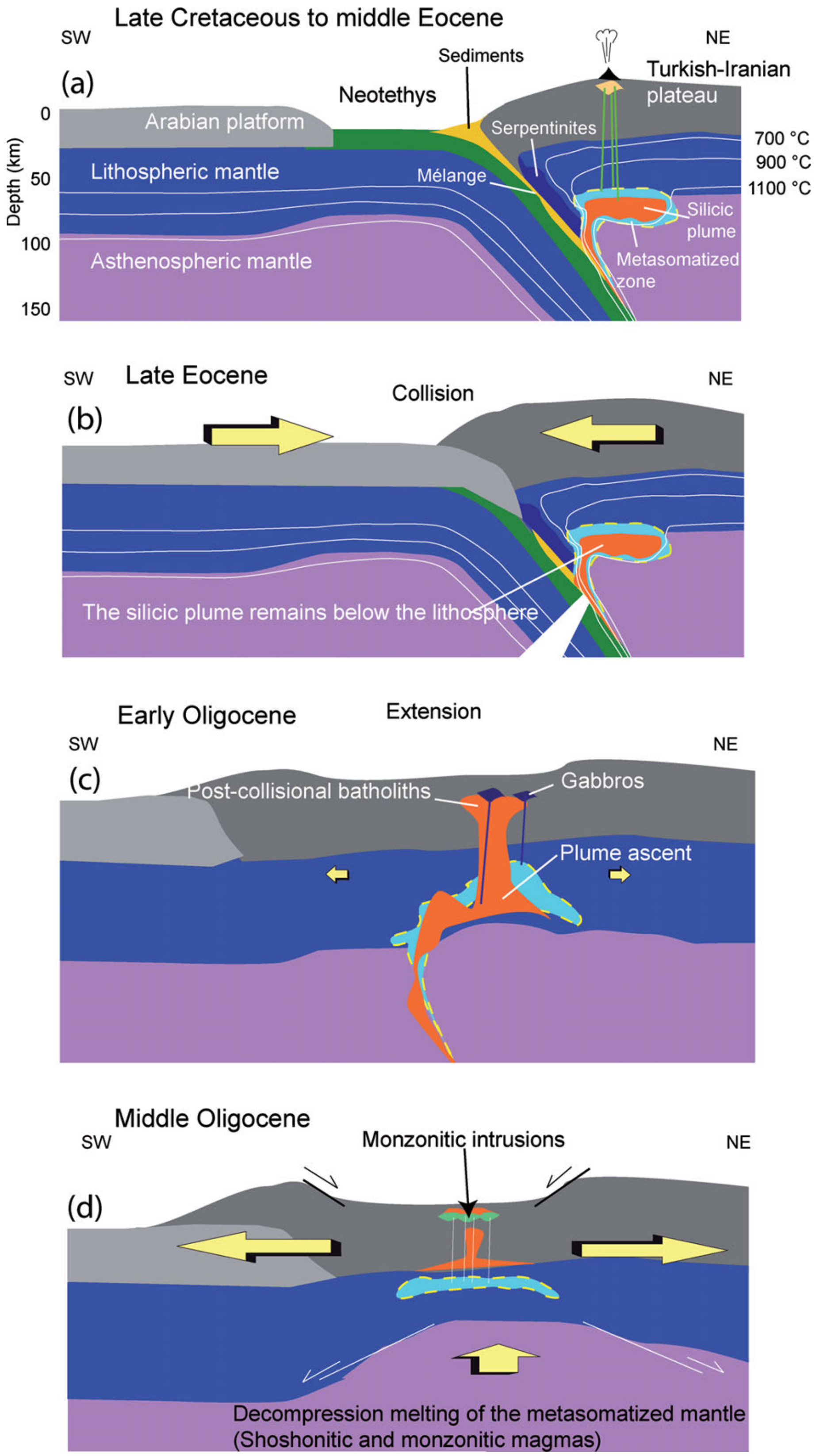

Figure 13. (Colour online) Cartoon showing possible loci of magma generation in a general context of lithosphere extension and pressure decrease in the source region of magmas. The first stage (a) is based on the results of numerical simulation of subduction at active continental margins. A tectonic mélange is formed by mixing subducted sediments and basalts. A buoyant silicic plume is formed and underplated below the lithosphere of the continental plate. Hypothetically, the compressive regime that characterizes this pre-collision stage will continue during continent–continent collision in Late Eocene time (b). Contracting structures are the dominant feature of crustal rocks that accommodate post-collisional batholiths. After collision, a generalized episode of post-orogenic relaxation allows the silicic plume to ascend and be emplaced within the lithosphere in the form of a large granitic batholith (c). Early Oligocene granite intrusions correspond to this stage. Continued extension may lead to decompression melting of previously metasomatized mantle peridotite giving rise to the generation of potassic magmatism of shoshonitic affinity (d) during the Middle Oligocene.

the mantle source (Foley & Wheller, 1990; Pearce & Parkinson, 1993). This is, however, not exclusive to the Zagros hinterland. Post-collisional, potassic magmatism with subduction-related geochemical signatures is a widespread feature of orogenic collisional orogens. According to thermomechanical models for subduction zones, referred to above, there is a minimum time delay of about 10 Ma between the initiation of the rheological perturbation, which leads to the generation of a cold plume from the subducting slab, and the time of plume emplacement into the continental hinterland. Further modelling is required to understand the dynamical and petrological processes involved in the transition from subduction to collision and post-collisional extension. However, according to the previous results and the timing of geological processes, it is expected that periods longer than 10 Ma can be found from the plume incubation period to the final emplacement. In the case of the Zagros orogen, studied here, the timing between subduction and collision is still poorly constrained, but important advances have been made in the last few years.

According to the Upper Palaeozoic–Lower Mesozoic strata in the SSMZ and Oman, it is stated that opening of the Neo-Tethys has been periodic (Stampfli, Marcoux & Baud, 1991; Ricou, 1994). These periods include initial rifting during Permian time. The main rifting phase, however, started in Triassic time. In the reconstructions by Şengör & Natal'in (1996) this ongoing Neo-Tethys Ocean started to subduct in Middle Jurassic time. Northwards subduction of the Neo-Tethyan ocean floor beneath Iran sutured Iran to Arabia (e.g. Takin, 1972; Berberian & King, 1981; Alavi, 1994), and the subsequent continental convergence built the Zagros orogenic belt. No consensus has yet been reached about the age of the first contact between the northern edge of Arabia and the margin of Eurasia. Age estimates for Arabia–Eurasia continent–continent collision indicate Late Cretaceous to Pliocene. According to Late Cretaceous obduction of ophiolitic sequences (e.g. Haynes & Reynolds, 1980) along the Zagros suture (e.g. Kermanshah and Neyriz ophiolites), some researchers consider collision between Arabia and Eurasia to occur at this time (Haynes & McQuillan, 1974; Stocklin, 1974; Berberian & Berberian, 1981; Alavi, 1994). However, many authors have related the Early Cenozoic intense magmatism along the UDMA, AMB and Central Iran with the time of collision at this or later periods during Middle Late Cenozoic time (e.g. Hempton, 1987; Hooper *et al.* 1994; Dewey & Şengör, 1979; Şengör & Kidd, 1979; Homke *et al.* 2004; McQuarrie *et al.* 2003; Stoneley, 1981; Philip *et al.* 1989; Allen & Armstrong, 2008; M. Aghazadeh, unpub. Ph.D. thesis, Tarbiat Modares Univ., 2009, among others). An Early Mesozoic age of collision between the Arabian and Eurasian continental blocks is supported by new data (Ghasemi & Talbot, 2006; Allen & Armstrong, 2008; Horton *et al.* 2008). Ghasemi & Talbot (2006) suggested an Early to Middle Eocene collision age for the Zagros suture. Horton *et al.* (2008), according to detrital zircon ages of Miocene strata in north-central Iran, stated that onset of the Arabia–Eurasia collision in Iran is between Middle Eocene and Late Oligocene time. Our data support a Late Eocene (40–35 Ma) age for the collision between Arabia and Eurasia in the NW Zagros. The age of collision can be taken as the time at which subduction was arrested. Consequently, a minimum delay between the time of the latest active subduction (40–35 Ma) and the time of post-collisional magmatism (30–23 Ma) of about 10 Ma is obtained for this sector of the Tethyan orogen. This time is within the range predicted by thermomechanical models. Thus, the application of these models makes compatible subduction geochemical fingerprints and post-collisional emplacement of the potassic magmas. Otherwise, it can be difficult to conceal both processes because subduction is not active at the time of magma emplacement.

9. Conclusions

The two magmatic cycles forming the Shaivar Dagh intrusive complex show typical geochemical signatures of subduction-related magmatism. The pluton is made up of two magmatic cycles with slight differences in time of only a few million years, but with marked differences in source composition. The earlier cycle is formed by calc-alkaline granodiorites and gabbros of clear cordilleran affinity. The later cycle is formed by massif monzonites and monzodiorites of shoshonitic affinity. The sources of the magmas of the two cycles were cooked during subduction below the active continental margin more than 10 Ma before final emplacement. A model based on the generation of silicic plumes in the mantle wedge and mantle metasomatism by melts derived from these plumes, is proposed. This interpretation has grounds in recently developed thermomechanical modelling of the mantle wedge during subduction at active continental margins.

Acknowledgements. We acknowledge with thanks the constructive reviews by Michael Haschke and Jeremy Richards. Dr Mark Allen made a careful addition to the manuscript. We thank Dr Andrea Dini for Sr and Nd isotope analyses at Istituto di Geoscienze e Georisorse – CNR, Pisa, Italy. This paper is part of the Ph.D. thesis of the first author supervised by M. H. Emami at the University of Tarbiat Modares. Financial support was received from Plan Andaluz de Investigación (Grant Proyecto de Excelencia RNM 5378).

References

Aghazadeh, M. 2006. *Geological Map of the Shaivar Dagh Intrusive Complex and Adjacent Area, 1:20,000 scale.* Tehran, Iran: Geological Survey of Iran.

Aghazadeh, M., Castro, A., Rashidnejad Omran, N., Emami, M. H., Moinvaziri, H. & Badrzadeh, Z. 2010. The gabbro (shoshonitic)–monzonite–granodiorite association of Khankandi pluton, Alborz Mountains, NW Iran. *Journal of Asian Earth Sciences* **38**, 199–219.

Ahmadian, J., Haschke, M., Mcdonald, I., Regelous, M., Ghorbani, M. H., Emami, M. H. & Murata, M.

2009. High magmatic flux during Alpine–Himalayan collision: constraints from the Kal-e-Kafi complex, central Iran. *Geological Society of America Bulletin* **121**, 857–68.

Ahmadzadeh, G., Jahangiri, A., Lentz, D. & Mojtahedi, M. 2010. Petrogenesis of Plio-Quaternary post-collisional ultrapotassic volcanism in NW of Marand, NW Iran. *Journal of Asian Earth Sciences* **39**, 37–50.

Ajaji, T., Weis, D., Giret, A. & Bouabdellah, M. 1998. Coeval potassic and sodic calc-alkaline series in the post-collisional Hercynian Tanncherfi intrusive complex, northeastern Morocco: geochemical, isotopic and geochronological evidence. *Lithos* **45**, 371–93.

Alavi, M. 1994. Tectonics of the Zagros orogenic belt of Iran: new data and interpretations. *Tectonophysics* **229**, 211–38.

Alavi, M. 1996. Tectonostratigraphic synthesis and structural style of the Alborz mountain system in northern Iran. *Journal of Geodynamics* **21**, 1–33.

Alavi, M. 2004. Regional stratigraphy of the Zagros fold-thrust belt of Iran and its proforeland evolution. *American Journal of Science* **304**, 1–20.

Alici, P., Temel, A., Gourgaud, A., Kieffer, G. & Gundogdu, M. N. 1998. Petrology and geochemistry of potassic rocks in the Golcuk area (Isparta, SW Turkey): genesis of enriched alkaline magmas. *Journal of Volcanology and Geothermal Research* **85**, 423–46.

Allen, M. B. & Armstrong, H. A. 2008. Arabia–Eurasia collision and the forcing of mid-Cenozoic global cooling. *Palaeogeography, Palaeoclimatology, Palaeoecology* **265**, 52–8.

Allen, M. B., Ghassemi, M. R., Shahrabi, M. & Qorashi, M. 2003. Accommodation of late Cenozoic shortening in the Alborz range, northern Iran. *Journal of Structural Geology* **25**, 659–72.

Alpaslan, M., Boztug, D., Frei, R., Temel, A. & Kurt, M. A. 2006. Geochemical and Pb–Sr–Nd isotopic composition of the ultrapotassic volcanic rocks from the extension-related Çamardı-Ulukışla basin, Niğde Province, Central Anatolia, Turkey. *Journal of Asian Earth Sciences* **27**, 613–27.

Amidi, S. M., Emami, M. H. & Michel, R. 1984. Alkaline character of Eocene volcanism in the middle part of Iran and its geodynamic situation. *Geologische Rundschau* **73**, 917–32.

Annells, R. N., Arthurton, R. S., Bazley, R. A. & Davies, R. G. 1975. *Explanatory Text of the Qazvin and Rasht Quadrangles Map, E3 and E4*. Tehran, Iran: Geological Survey of Iran, pp. 94.

Azizi, H. & Moinvaziri, H. 2009. Review of the tectonic setting of Cretaceous to Quaternary volcanism in northwestern Iran. *Journal of Geodynamics* **47**, 167–79.

Babakhani, A. R., Lesquyer, J. L. & Rico, R. 1990. *Geological Map of Ahar Quadrangle (scale 1:250,000)*. Tehran, Iran: Geological Survey of Iran.

Bea, F., Montero, P. G., Gonzalez-Lodeiro, F. & Talavera, C. 2007. Zircon inheritance reveals exceptionally fast crustal magma generation processes in Central Iberia during the Cambro-Ordovician. *Journal of Petrology* **48**, 2327–39.

Bea, F., Montero, P. G., Talavera, C. & Zinger, T. 2006. A revised Ordovician age for the oldest magmatism of Central Iberia: U-Pb ion microprobe and LA-ICPMS dating of the Miranda do Douro orthogneiss. *Geologica Acta* **4**, 395–401.

Berberian, M. 1983. The southern Caspian: a compressional depression floored by a trapped, modified oceanic crust. *Canadian Journal of Earth Sciences* **20**, 163–83.

Berberian, F. & Berberian, M. 1981. Tectono-plutonic episodes in Iran. In *Zagros, Hindu Kush, Himalaya Geodynamic Evolution*, vol 3 (eds H. K. Gupta & F. M. Delany), pp. 5–32. Washington, D.C.: American Geophysical Union.

Berberian, M. & King, G. C. P. 1981. Towards a paleogeography and tectonic evolution of Iran. *Canadian Journal of Earth Sciences* **18**, 210–65.

Berberian, F., Muir, I. D., Pankhurst, R. J. & Berberian, M. 1982. Late Cretaceous and early Miocene Andean type plutonic activity in northern Makran and central Iran. *Journal of the Geological Society, London* **139**, 605–14.

Castro, A. & Gerya, T. V. 2008. Magmatic implications of mantle wedge plumes: experimental study. *Lithos* **103**, 138–48.

Castro, A., Gerya, T., Garcia-Casco, A., Fernandez, C., Diaz-Alvarado, J., Moreno-Ventas, I. & Löw, I. 2010. Melting relations of MORB-sediment melanges in underplated mantle wedge plumes. Implications for the origin of Cordilleran-type batholiths. *Journal of Petrology* **51**, 1267–95.

Conceição, R. V. & Green, D. H. 2004. Derivation of potassic (shoshonitic) magmas by decompression melting of phlogopite + pargasite lherzolite. *Lithos* **72**, 209–29.

Conticelli, S., Guarnieri, L., Farinelli, A., Mattei, M., Avanzinelli, R., Bianchini, G., Boari, E., Tommasini, S., Tiepolo, M., Prelević, D. & Venturelli, G. 2009. Trace elements and Sr-Nd-Pb isotopes of K-rich, shoshonitic, and calc-alkaline magmatism of the Western Mediterranean Region: genesis of ultrapotassic to calc-alkaline magmatic associations in a post-collisional geodynamic setting. *Lithos* **107**, 68–92.

Conticelli, S. & Peccerillo, A. 1992. Petrology and geochemistry of potassic and ultrapotassic volcanism in central Italy: petrogenesis and inferences on the evolution of the mantle sources. *Lithos* **28**, 221–40.

Dercourt, J., Zonenshain, L., Rico, L. E., Kazmin, G., Lepichon, X., Knipper, A. L., Grandjacquet, C., Sbortshikov, I. M., Geyssant, J., Lepvrier, C., Pechersky, D. H., Boulin, J., Sibuet, J. C, Savostin, L. A., Sorokhtin, O., Westphal, M., Bazhenov, M. L., Lauer, J. P. & Biju-Duval, B. 1986. Geological evolution of the Tethys belt from the Atlantic to Pamirs since the Lias. *Tectonophysics* **123**, 241–315.

Dewey, J. F. & Şengör, A. M. C. 1979. Aegean and surrounding regions: complex multiplate and continuum tectonics in a convergent zone. *Geological Society of America Bulletin* **90**, 84–92.

Dilek, Y., Imamverdiyev, N. & Altunkaynak, S. 2009. Geochemistry and tectonics of Cenozoic volcanism in the Lesser Caucasus (Azerbaijan) and the peri-Arabian region: collision-induced mantle dynamics and its magmatic fingerprint. *International Geology Review* **52**, 536–78.

Eklund, O., Konopelko, D., Rutanen, H., Frodjo, S. & Shebanov, A. D. 1998. 1.8 Ga Svecofennian post-collisional shoshonitic magmatism in the Fennoscandian Shield. *Lithos* **45**, 87–108.

Elburg, M. A., Van Bergen, M., Hoogewerff, J., Foden, J., Vroon, P., Zulkarnian, I. & Nasution, A. 2002. Geochemical trends across an arc-continent collision zone: magma sources and slab-wedge transfer processes below the Pantar Strait volcanoes, Indonesia. *Geochimica et Cosmochimica Acta* **66**, 2771–89.

Foley, S. F. & Wheller, G. E. 1990. Parallels in the origin of the geochemical signatures of island arc volcanics and continental potassic igneous rocks: the role of residual titanites. *Chemical Geology* **85**, 1–18.

Fowler, M. B. 1992. Elemental and O-Sr-Nd isotope geochemistry of the Glen Dessary syenite, NW Scotland. *Journal of the Geological Society, London* **149**, 209–20.

Fowler, M. B., Kocks, H., Darbyshire, D. P. F. & Greenwood, P. B. 2008. Petrogenesis of high Ba–Sr plutons from the Northern Highlands Terrane of the British Caledonian Province. *Lithos* **105**, 129–48.

Frost, B. R., Arculus, R. J., Barenes, C. G., Collins, W. J., Ellis, D. J. & Frost, C. D. 2001. A geochemical classification of granitic rock suites. *Journal of Petrology* **42**, 2033–48.

Gao, Y., Yang, Z., Hou, Z., Wei, R., Meng, X. & Tian, S. 2010. Eocene potassic and ultrapotassic volcanism in south Tibet: new constraints on mantle source characteristics and geodynamic processes. *Lithos* **11**, 20–32.

Gerya, T. V. & Yuen, D. A. 2003. Rayleigh–Taylor instabilities from hydration and melting propel “cold plumes” at subduction zones. *Earth and Planetary Science Letters* **212**, 47–62.

Gerya, T. V., Yuen, D.A. & Sevre, E. O. D. 2004. Dynamical causes for incipient magma chambers above slabs. *Geology* **32**, 89–92.

Ghasemi, A. & Talbot, C. J. 2006. A new tectonic scenario for the Sanandaj–Sirjan zone (Iran). *Journal of Asian Earth Sciences* **26**, 683–93.

Ghiorso, M. S. & Sack, R. O. 1995. Chemical mass transfer in magmatic processes. IV. A revised and internally consistent thermodynamic model for the interpolation and extrapolation of liquid–solid equilibria in magmatic systems at elevated temperatures and pressures. *Contributions to Mineralogy and Petrology* **119**, 197–212.

Green, D. H. 1973. Experimental studies on a model upper mantle composition at high pressure under water-undersaturated and water-saturated conditions. *Earth and Planetary Science Letters* **19**, 37–53.

Harris, N. B. W., Pearce, J. A., & Tindele, A. G. 1986. Geochemical characteristics of collision-zone magmatism. In *Collision Tectonics* (eds M. P. Coward & A. C. Ries), pp. 67–82. Geological Society of London, Special Publication no. 19.

Haschke, M. & Ben-Avraham, Z. 2005. Adakites from collision-modified lithosphere. *Geophysical Research Letters* **32**, L15302, doi:10.1029/2005GL023468, 4 pp.

Haschke, M., Ahmadian, J., Murata, M. & McDonald, I. 2010. Copper mineralization prevented by arc-root delamination during Alpine-Himalayan collision in central Iran. *Economic Geology* **105**, 855–65.

Hassanzadeh, J., Ghazi, A. M., Axen, G. & Guest, B. 2002. Oligo-Miocene mafic alkaline magmatism north and northwest of Iran: evidence for the separation of the Alborz from the Urumieh-Dokhtar magmatic arc. *Geological Society of America Abstracts with Programs* **34**, 331.

Hawkesworth, C. J., Turner, S. P., Mcdermott, F., Peate, D. W. & Van Calsteren, P. 1997. U, Th isotopes in arc magmas: implications for element transfer from the subducted crust. *Science* **276**, 551–5.

Haynes, S. J. & McQuillan, H. 1974. Evolution of the Zagros suture zone, southern Iran. *Geological Society of America Bulletin* **85**, 739–44.

Haynes, S. J. & Reynolds, P. H. 1980. Early development of Tethys and Jurassic ophiolite displacement. *Nature* **283**, 560–3.

Hempton, M. R. 1987. Constraints on Arabian plate motion and extensional history of the Red Sea. *Tectonics* **6**, 687–705.

Holden, P., Halliday, A. N. & Stephens, W. E. 1987. Neodymium and strontium isotope content of microdiorite enclaves points to mantle input to granitoid production. *Nature* **330**: 53–6.

Homke, S., Verges, J., Garces, M., Emami, M. & Karpuz, R. 2004. Magnetostratigraphy of Miocene–Pliocene Zagros foreland deposits in the front of the Push-e-Kush Arc (Lurestan Province, Iran). *Earth and Planetary Science Letters* **225**, 397–410.

Hooper, R. J., Baron, I. R., Agah, S. & Hatcher, R. D. 1994. The Cenomanian to recent development of the Southern Tethyan Margin in Iran. In *Middle East Petroleum Geosciences GEO 94*, vol 2 (ed. M. I. Al-Husseini), pp. 505–16. Bahrain: Gulf PetroLink.

Horton, B. K., Hassanzadeh, J., Stockli, D. F., Axen, G. J., Gillis, R. J., Guest, B., Amini, A., Fakhari, M. D., Zamanzadeh, S. M. & Grove, M. 2008. Detrital zircon provenance of Neoproterozoic to Cenozoic deposits in Iran: implications for chronostratigraphy and collisional tectonics. *Tectonophysics* **451**, 97–122.

Jahangiri, A. 2007. Post-collisional Miocene adakitic volcanism in NW Iran: geochemical and geodynamic implications. *Journal of Asian Earth Sciences* **30**, 433–47.

Johnson, M. C. & Rutherford, M. J. 1989. Experimental calibration of the aluminum-in-hornblende geobarometer with application to Long Valley caldera (California) volcanic rocks. *Geology* **17**, 837–41.

Keskin, M. 2003. Magma generation by slab steepening and breakoff beneath a subduction-accretion complex: an alternative model for collision-related volcanism in Eastern Anatolia, Turkey. *Geophysical Research Letters* **30**, 8046, doi:10.1029/2003GL018019, 4 pp.

Khain, V. E. 1977. Critical composition of mobilistic models of tectonic development of the Caucasus. In *International Symposium of the Mediterranean Basins, Split (Yugoslavia)* (eds B. Biju-Duval & L. Montadert), pp. 353–62.

Kheirkhah, M., Allen, M. B. & Emami, M. H. 2009. Quaternary syn-collision magmatism from the Iran/Turkey borderlands. *Journal of Volcanology and Geothermal Research* **182**, 1–12.

Küster, D. & Harms, U. 1998. Post-collisional potassic granitoids from the southern and northwestern parts of the Late Neoproterozoic East African Orogen: a review. *Lithos* **45**, 177–95.

Le Maitre, R. W. 2002. *Igneous Rocks – A Classification and Glossary of Terms*. Cambridge: Cambridge University Press, 236 pp.

López-Moro, F. J. & López-Plaza, M. 2004. Monzonitic series from the Variscan Tormes Dome (Central Iberian Zone): petrogenetic evolution from monzogabbro to granite magmas. *Lithos* **72**, 19–44.

McQuarrie, N., Stock, J. M., Verdel, C. & Wernicke, B. P. 2003. Cenozoic evolution of Neotethys and implications for the causes of plate motions. *Geophysical Research Letters* **30**, 2036, doi:10.1029/2003GL017992, 4 pp.

Mohajjel, M. & Fergusson, C. L. 2000. Dextral transpression in Late Cretaceous continental collision, Sanandaj–

Sirjan Zone, Western Iran. *Journal of Structural Geology* **22**, 1125–39.

Mohajjel, M., Fergusson, C. L. & Sahandi, M. R. 2003. Cretaceous–Tertiary convergence and continental collision, Sanandaj–Sirjan Zone, western Iran. *Journal of Asian Earth Sciences* **4**, 397–412.

Montero, P., Bea, F., Gonzalez-Lodeiro, F., Talavera, C. & Whitehouse, M. 2007. Zircon ages of the metavolcanic rocks and metagranites of the Ollo de Sapo Domain in central Spain: implications for the Neoproterozoic to Early Palaeozoic evolution of Iberia. *Geological Magazine* **144**, 963–76.

Morimoto, N. 1988. Nomenclature of pyroxenes. *Mineralogy and Petrology* **66**, 237–52.

Morrison, G. W. 1980. Characteristics and tectonic setting of the shoshonite rock association. *Lithos* **13**, 97–108.

Niida, K. & Green, D. H. 1999. Stability and chemical composition of pargasitic amphibole in MORB pyrolite under upper mantle conditions. *Contributions to Mineralogy and Petrology* **135**, 18–40.

Omrani, J., Agard, P., Whitechurch, H., Benoit, M., Prouteau, G. & Jolivet, L. 2008. Arc-magmatism and subduction history beneath the Zagros Mountains, Iran: a new report of adakites and geodynamic consequences. *Lithos* **106**, 380–98.

Pearce, J. A. 1983. Role of the sub-continental lithosphere in magma genesis at active continental margins. In *Continental Basalts and Mantle Xenoliths* (eds C. J. Hawkesworth & M. J. Norry), pp. 230–50. Nantwich, Cheshire, UK: Shiva.

Pearce, J. A., Bender, J. F. & De Long, S. E. 1990. Genesis of collision volcanism in Eastern Anatolia, Turkey. *Journal of Volcanology and Geothermal Research* **44**, 189–229.

Pearce, J. A., Harris, N. B. & Tindle, A. G. 1984. Trace element discrimination diagrams for the tectonic interpretation of granitic rocks. *Journal of Petrology* **25**, 956–83.

Pearce, J. A. & Parkinson, I. J. 1993. Trace element models for mantle melting: application to volcanic arc petrogenesis. In *Magmatic Processes and Plate Tectonics* (eds H. M. Prichard, T. Alabaster, N. B. W. Harris & C. R. Neary), pp. 373–403. Geological Society of London, Special Publication no. 76.

Philip, H., Cisternas, A., Gvishiani, A. & Gorshkov, A. 1989. The Caucasus: an actual example of the initial stages of continental collision. *Tectonophysics* **161**, 1–21.

Pitcher, W. S. 1997. *The Nature and Origin of Granite*. London: Blackie, 321 pp.

Ricou, L. E. 1994. Tethys reconstructed: plates, continental fragments and their boundaries since 260 Ma from Central America to South-eastern Asia. *Geodinamica Acta* **7**, 169–218.

Robertson, A. H. F. 2000. Mesozoic–Tertiary tectonic-sedimentary evolution of a south Tethyan oceanic basin and its margins in southern Turkey. In *Tectonics and Magmatism in Turkey and the Surrounding Area* (eds E. Bozkurt, J. A. Winchester & J. D. A. Piper), pp. 97–138. Geological Society of London, Special Publication no. 173.

Scarrow, J. H., Molina, J. F., Bea, F. & Montero, P. 2009. Within-plate calc-alkaline rocks: insights from alkaline mafic magma-peraluminous crustal melt hybrid appinites of the Central Iberian Variscan continental collision. *Lithos* **110**, 50–64.

Schmidt, M. W. 1992. Amphibole composition in tonalite as a function of pressure: an experimental calibration of the Al-in-hornblende barometer. *Contributions to Mineralogy and Petrology* **110**, 304–10.

Şengör, A. M. C. & Kidd, W. S. F. 1979. Post-collisional tectonics of the Turkish–Iranian plateau and a comparison with Tibet. *Tectonophysics* **55**, 361–76.

Şengör, A. M. C. & Natal'in, B. A. 1996. Paleotectonics of Asia: fragments of the synthesis. In *The Tectonic Evolution of Asia* (eds A. Yin & T. M. Harrison), pp. 486–640. Cambridge: Cambridge University Press.

Shafiei, B., Haschke, M. & Shahabpour, J. 2009. Recycling of orogenic arc crust triggers porphyry Cu mineralization in Kerman Cenozoic arc rocks, southeastern Iran. *Mineralium Deposita* **44**, 265–83.

Shahabpour, J. 2007. Island arc affinity of the central Iranian belt. *Journal Asian Earth Science* **30**, 652–65.

Sizova, E., Gerya, T., Brown, M. & Perchuk, L. L. 2010. Subduction styles in the Precambrian: insight from numerical experiments. *Lithos* **116**, 209–29.

Stampfli, G. M. 2000. Tethyan oceans. In *Tectonics and Magmatism in Turkey and Surrounding Area* (eds E. Bozkurt, J. A. Winchester & J. D. A. Piper), pp. 1–23. Geological Society of London, Special Publication no. 173.

Stampfli, G., Marcoux, J. & Baud, A. 1991. Tethyan margins in space and time. *Palaeogeography, Palaeoclimatology, Palaeoecology* **87**, 373–409.

Stephens, W. E. & Halliday, A. N. 1984. Geochemical contrasts between late Caledonian granitoid plutons of northern, central and southern Scotland. *Transactions of the Royal Society of Edinburgh: Earth Sciences* **75**, 259–73.

Stocklin, J. 1974. Possible ancient continental margins in Iran. In *The Geology of Continental Margins* (eds C. A. Burk, & C. L. Drake), pp. 873–87. Berlin: Springer.

Stoneley, R. 1981. The geology of the Kuh-e Dalneshim area of southern Iran, and its bearing on the evolution of southern Tethys. *Journal of the Geological Society, London* **138**, 509–26.

Takin, M. 1972. Iranian geology and continental drift in the Middle East. *Nature* **23**, 147–50.

Tatsumi, Y. 1989. Migration of fluid phases and genesis of basalt magmas in subduction zones. *Journal of Geophysical Research* **94**, 4697–707.

Thompson, A. B. 1992. Water in the Earth's upper mantle. *Nature* **358**: 295.

Topuz, G., Altherr, R., Schwarz, W. H., Siebel, W., Satir, M. & Dokuz, A. 2005. Post-collisional plutonism with adakite-like signatures: the Eocene Saraycık granodiorite (Eastern Pontides, Turkey). *Contributions to Mineralogy and Petrology* **150**, 441–55.

Turner, S., Arnaud, N., Liu, J., Rogers, N., Hawesworth, C., Harris, N., Kelley, S., Van Calsteren, P. & Deng, W. 1996. Postcollision, shoshonitic volcanism on the Tibetan Plateau: implications for convective thinning of the lithosphere and the source of ocean island basalts. *Journal of Petrology* **37**, 45–71.

Venturelli, G., Thorpe, R. S., Dal Piaz, G. V., Del Moro, A. & Potts, P. J. 1984. Petrogenesis of calc-alkaline, shoshonitic and associated ultrapotassic Oligocene volcanic rocks from the Northwestern Alps, Italy. *Contributions to Mineralogy and Petrology* **86**, 209–20.

WANG, Q., LI, J. W., JIAN, P., ZHAO, Z. H., XIONG, X. L., BAO, Z. W., XU, J. F., LI, C. F. & MA, J. L. 2005*a*. Alkaline syenites in eastern Cathaysia (South China): link to Permian–Triassic transtension. *Earth and Planetary Science Letters* **230**, 339–54.

WANG, Q., MCDERMOTT, F., XU, J. F., BELLON, H. & ZHU, Y. T. 2005*b*. Cenozoic K-rich adakitic volcanics in the Hohxil area, northern Tibet: lower crustal melting in an intracontinental setting. *Geology* **33**, 465–8.

WANG, Q., WYMAN, D. A., XU, J. F., ZHAO, Z. H., JIAN, P., XIONG, X. L., BAO, Z. W., LI, C. F. & BAI, Z. H. 2006. Petrogenesis of Cretaceous adakitic and shoshonitic igneous rocks in the Luzong area, Anhui Province (eastern China): implications for geodynamics and Cu-Au mineralization. *Lithos* **89**, 424–46.

WANG, Q., XU, J. F., ZHAO, Z. H., BAO, Z. W., XU, W. & XIONG, X. L. 2004*a*. Cretaceous high-potassium intrusive rocks in the Yueshan–Hongzhen area of east China: adakites in an extensional tectonic regime within a continent. *Geochemical Journal* **38**, 417–34.

WANG, Q., ZHAO, Z. H., BAO, Z. W., XU, J. F., LIU, W. & LI, C. F. 2004*b*. Geochemistry and petrogenesis of the Tongshankou and Yinzu adakitic intrusive rocks and the associated porphyry copper-molybdenum mineralization in southeast Hubei, east China. *Resource Geology* **54**, 137–52.

WATSON, E. B. & HARRISON, T. M. 2005. Zircon thermometer reveals minimum melting conditions on earliest Earth. *Science* **308**, 841–4.

WILLIAMS, H. M., TURNER, S. P., PEARCE, J. A., KELLEY, S. P. & HARRIS, N. B. W. 2004. Nature of the source regions for postcollisional, potassic magmatism in southern and northern Tibet from geochemical variations and inverse trace element modeling. *Journal of Petrology* **45**, 555–607.

XIAO, L. & CLEMENS, J. D. 2007. Origin of potassic (C-type) adakite magmas: experimental and field constraints. *Lithos* **95**, 399–414.

XU, J. F., SHINJIO, R., DEFANT, M. J., WANG, Q. & RAPP, R. P. 2002. Origin of Mesozoic adakitic intrusive rocks in the Ningzhen area of east China: partial melting of delaminated lower continental crust? *Geology* **12**, 1111–14.

YANG, J. H., CHUNG, S. L., WILDE, S. A., WU, F. Y., CHU, M. F., LO, C. H. & FAN, H. R. 2005. Petrogenesis of post-orogenic syenites in the Sulu Orogenic Belt, East China: geochronological, geochemical and Nd–Sr isotopic evidence. *Chemical Geology* **214**, 99–125.

YILMAZ, Y. 1993. New evidence and model on the evolution of the southeast Anatolian orogen. *Geological Society of America Bulletin* **105**, 251–71.

ZINDLER, A. & HART, S. 1986. Chemical geodynamics. *Annual Review of Earth and Planetary Sciences* **14**, 493–571.